Fabricating Off-Plane Reflection Gratings for Use in a Rocket-Bourne X-ray Spectrometer

Casey T. DeRoo

January 21, 2015

Contents

Chapter 1

Introduction

1.1 X-ray Grating Spectroscopy

The soft X-ray energy range (0.3 – 1.5 keV) is host to a number of transition lines helpful in characterizing astrophysical plasmas in energetic environments. Stellar coronae, black hole accretion disks, supernova remnants, and the intergalactic medium are all examples of environments that can be probed with soft X-ray spectroscopy. Highly resolved spectra with good signal-to-noise can be used to determine the temperature, density, ionization state, and metallicity of the plasma in these environments and provide important constraints on physical models.

The instrument of choice for obtaining spectra from these sources is an X-ray grating spectrometer[1]. X-ray grating spectrometers typically consist of three major components: a telescope, a grating array, and a detector array. The telescope, usually of nested Wolter-I type, collects light from the source and directs it towards a focus several meters down the optical axis. Instead of being allowed to reach the focus, however, the converging light is intercepted by a grating array placed directly after the telescope. The periodic structure present on the gratings diffracts the converging light based on wavelength. The diffraction pattern is then imaged with a detector array at the focal plane, and the source spectrum is reconstructed based on the observed diffraction pattern.

X-ray grating spectrometers typically fall into three major categories based on the

[1]Microcalorimeters are a promising technology for X-ray spectroscopy at higher energies; however, their resolving power scales with photon energy. Hence, microcalorimeters perform poorly at energies < 1.0 keV. Grating spectrometers, on the other hand, have a resolving power that grows with wavelength, meaning that resolutions of several thousand can be achieved in the soft X-ray bandpass.

kind of grating employed: transmission, in-plane reflection, and off-plane reflection (Figure 1.1). A typical X-ray transmission grating is a periodic structure of 'slatted' bars held in place by a support architecture which permits photons to pass through. In-plane X-ray reflection gratings are very similar to a standard optical grating; periodically spaced grooves run perpendicular to the incoming light, resulting in a far-field diffraction pattern in the plane defined by the grating normal and the direction of the incoming light (hence, 'in-plane'). Off-plane gratings are similar to in-plane gratings, save that the grating grooves are oriented quasi-parallel to the incoming light. This results in a conical diffraction pattern at the focal plane, sometimes called the 'arc of diffraction.' Through shaping of the groove facet, in-plane and off-plane reflection gratings can be made to 'blaze,' or achieve high efficiency in a given order based on diffraction geometry.

The geometry of the off-plane mount offers several distinct advantages over its counterparts in an astrophysical context (Cash (1991)). The largest advantage gained from off-plane gratings over in-plane gratings is that off-plane gratings do not suffer from vignetting at high order. The resolving power of a grating spectrometer increases when working at higher order, scaling linearly with n, the order number. Stacking gratings at grazing incidence to form an array, a technique common for increasing collecting area in X-ray spectrometers, can result in vignetting for gratings in the in-plane mount, since higher orders are dispersed upwards into the grating above. The off-plane mount, however, disperses high orders out of the plane of incidence where there is no impediment along the optical path. Both in-plane and off-plane gratings have the advantage that they are usually studier than transmission gratings, making them less susceptible to failure under launch loads. Transmission gratings must also employ a support structure to reinforce the vertical bars, which comes at the expense of effective collecting area for the grating array. Finally, both in-plane and off-plane gratings are traditionally easier to fabricate than transmission gratings. For these reasons, we specifically consider off-plane variants for future spectrometers.

1.2 Off-Plane Grating Diffraction Geometry

Since the source spectrum is ultimately reconstructed from the recorded spatial distribution of photons at the focal plane, it is important to have a clear mathematical understanding of off-plane diffraction geometry. In the off-plane mount (Figure 1.2), incoming light approaches nearly parallel to the grating grooves. In the X-ray, the incidence angle γ must be shallow, typically between 1° – 2°, as X-ray reflectivity falls off rapidly at higher angles. In the off-plane mount, the grating equation is:

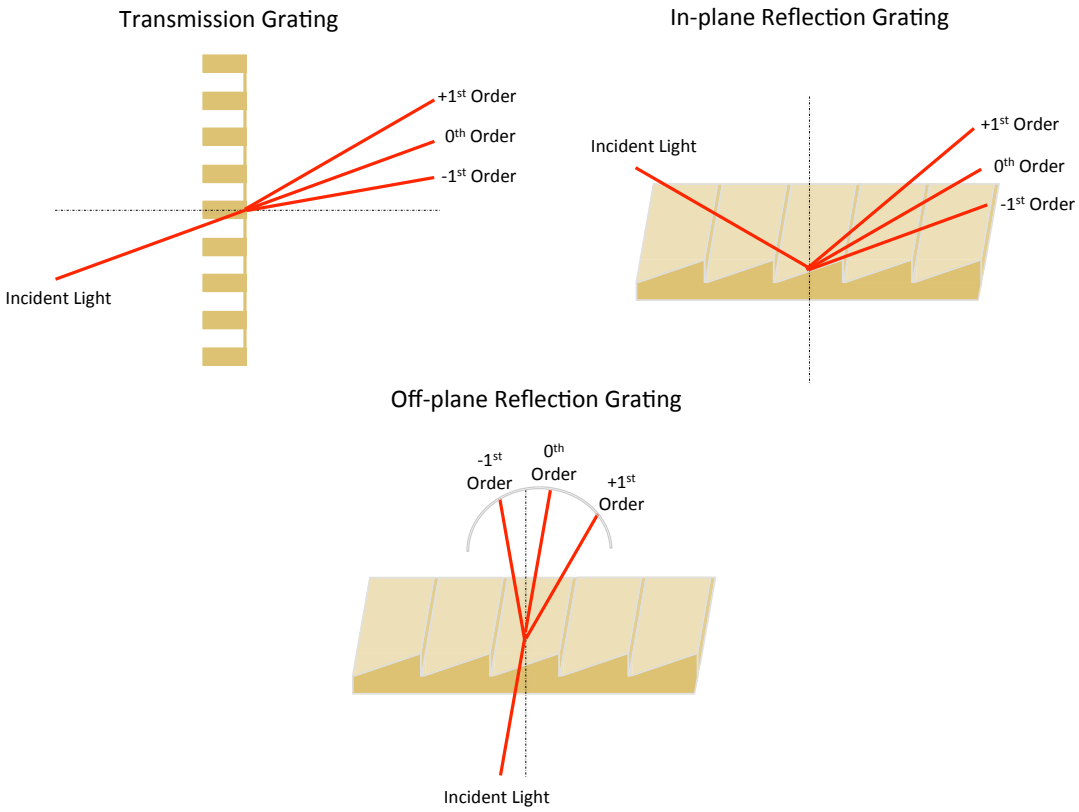

Figure 1.1: The diffraction pattern for transmission (*Top Left*), in-plane reflection (*Top Right*), and off-plane reflection gratings (*Bottom*).

$$\sin\alpha + \sin\beta = \frac{n\lambda}{\mathrm{d}\sin\gamma}, \tag{1.1}$$

where d is the groove period, λ is the wavelength of the diffracting photon, α is the azimuthal angle between the zero order spot and the grating normal projected into the focal plane, β is the azimuthal angle between the diffracted spot and the grating normal projected into the focal plane, and n is the order number. Other parameters relevant to the position of the diffracted spots are L, the linear distance between the grating and the focal plane, which sets the physical scale of the system and is often called the 'throw,' and θ, the facet angle of a blazed grating. By taking the deviative of the grating equation with respect to λ and noting that $\mathrm{dx} = L\sin\gamma\cos\beta\,\mathrm{d}\beta$, it can be shown that:

$$\frac{\mathrm{d}\lambda}{\mathrm{dx}} = \frac{10^7\,\frac{\text{Å}}{\text{mm}}}{nL\mathrm{D}}, \tag{1.2}$$

where $\mathrm{D} \equiv 1/\mathrm{d}$, the groove density. Equation 1.2 hence implies that the linear distance dispersed from zero order is proportional to the wavelength of the incoming light for a given order. Though diffracted orders are constrained to appear on the arc of diffraction according to Equation 1.1, it is not necessary to know the full two-dimensional position of the diffracted spot; only the x dimension is needed for spectral reconstruction of the source. The resolution R of such an instrument is then the distance dispersed from zero order divided by the uncertainty in the position of line[2]. The resolving power of the spectrometer thus comes down to how well the position of the diffracted spot is known relative to zero order - in essence:

$$R = \frac{\lambda}{\Delta\lambda} = \frac{\mathrm{x}}{\Delta\mathrm{x}}. \tag{1.3}$$

The relationship between physical space and wavelength space, $\mathrm{d}\lambda/\mathrm{dx}$, (Equation 1.2) is often called the dispersion of the spectrometer. Smaller dispersions, achieved by higher groove densities or a longer 'throw' from the grating to the focal plane, serve to spread the source spectrum out over a greater linear distance, increasing[3] the spectral resolving power of the instrument while requiring a larger focal plane in order to image the same bandpass.

[2]Free of system-induced aberration, this reduces to the physical extent of the linespread function of the telescope in the direction of dispersion. Hence, the quality of the focus achieved by the X-ray telescope is a direct factor in determining the resolution of the system.

[3]Given no change in the linespread function over this increased dispersion distance. In practice, the increase in distance dispersed is often offset by a blurring of the linespread function owing to added optical path length. Thus, a careful study of the optical system is required.

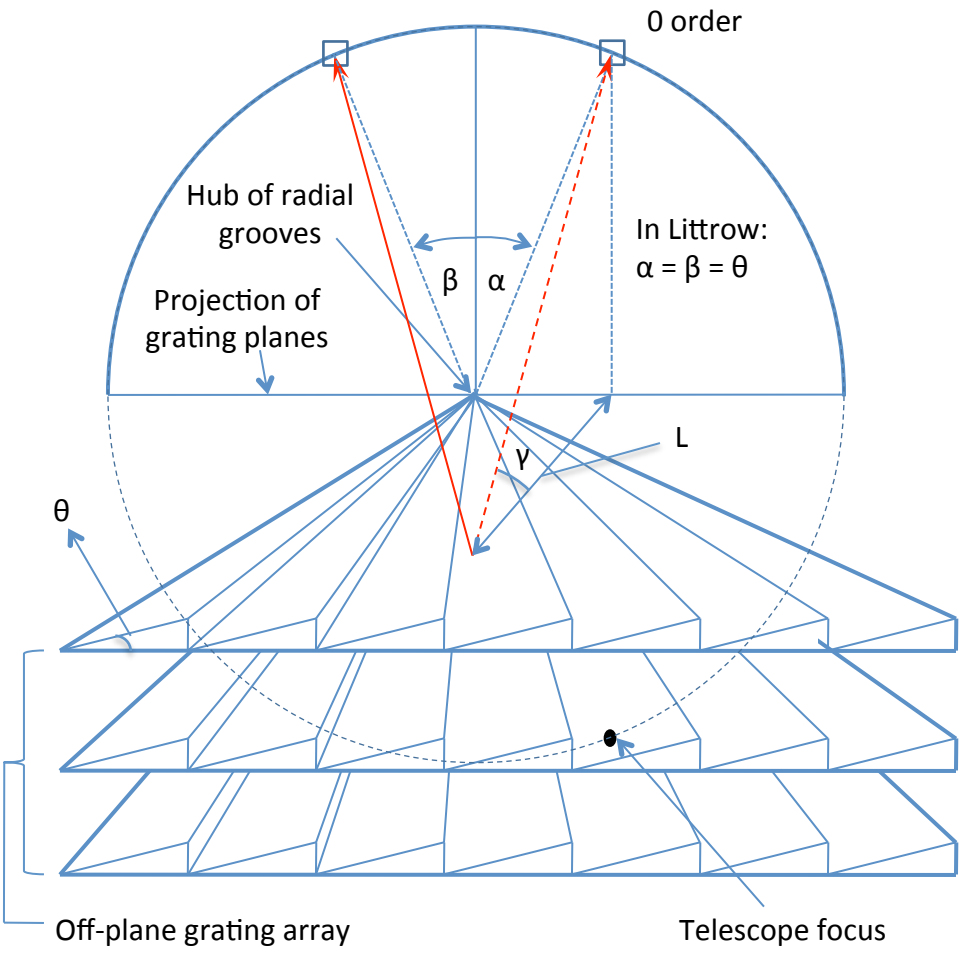

Figure 1.2: The geometry of the off-plane mount.

1.3 Current Instruments and Future Needs

Gratings are employed on the currently operating *Chandra X-ray Observatory* and *XMM-Newton* to obtain soft X-ray spectra, and have demonstated the importance of high resolution X-ray spectroscopy during their lifetimes. However, both of these facilities are now fifteen years old and not able to perform the measurements needed for next-generation science. The *Chandra* High Energy Transmission Grating (HETG) Spectrometer employs transmission gratings and is capable of resolutions ($\lambda/\Delta\lambda$) of up to several hundred on bright sources, with effective collecting areas of 7 – 200 cm^2 from 0.5 – 1.5 keV (*Chandra* Project Science, MSFC (2014)) The *Chandra* Low Energy Transmission Grating (LETG) Spectrometer operates at slighly lower energies, sampling energies from 0.2 – 1.0 keV with effective areas of < 20 cm^2 and obtaining resolutions of 1000 – 100 (@ 0.2 and 1.0 keV respectively). *XMM*, on the other hand, uses in-plane reflection gratings, has slightly better effective area (up to 70 cm^2, with > 20 cm^2 over the entire 0.3 – 1.5 keV range), and obtains resolutions up to $\sim$500 (den Herder et al., 2001).

In contrast, resolutions of multiple thousands and effective areas of hundreds of square centimeters are needed to perform some of the key science in high energy environments. For example, understanding the formation of large-scale structure in the universe requires probing the filamentary structures between galaxy clusters (sometimes referred to as the 'cosmic web'). This material is known as the Warm-Hot Intergalactic Medium (WHIM), and can be observed in absorption along the sightlines of active galactic nuclei (AGN). Of particular importance for WHIM studies is the OVII resonance line @ $\lambda = 21.60$ Å, from which the column density of metal[4]-enriched material along the line of sight can be inferred.

The ability of a spectrometer to detect an isolated feature like the OVII resonance line scales with:

$$S/N \propto \left[A_{\rm eff}(E)R(E)\right]^{0.5}, \tag{1.4}$$

where $A_{\rm eff}(E)$ is the effective area of the instrument at energy E and $R(E)$ is the resolution of the instrument at energy E and S/N is the signal-to-noise ratio of the line (*Chandra* Project Science, MSFC, 2014, Sec. 8.5.4). The signal-to-noise ratios of *Chandra* and *XMM* are too low to resolve the OVII absorption signal from the WHIM by a factor of 2 – 6 (Bregman, 2007). When folded with the effective areas and resolutions of these instruments at 21.60 Å, resolving the WHIM OVII resonance line necessarily implies a spectrometer with $R > 1000$ and $A_{\rm eff} > 100$ cm^2.

[4]Note that in the astronomical sense, all elements besides H and He are considered metals.

Such a spectrometer would also significantly advance the study of stellar physics. By measuring the emission line flux and line width of C, N, O, Ne, Fe emission lines, it is possible to map the density, temperature and turbulent velocity of shock and post-shock material from an accretion flow onto a young star. These measurements would enable the understanding of stellar accretion physics beyond the basic accretion shock model, but require R > 1000 and a minimum effective area of $A_{\rm eff} = 200$ cm^2 (Smith, 2014b). X-ray spectroscopy studies of the stellar coronae measuring dielectronic recombination (DR) lines, which are sensitive to temperature and density in the recombining plasma, can help to differentiate between coronal heating models. DR lines, however, are satellite lines and weak in comparison to the resonance lines also present in the source spectrum. Measuring DR lines requires having sufficient energy resolution to separate them from stronger features and the signal-to-noise to gather adequate statistics for analysis. This again implies resolutions on the order of thousands and effective areas of greater than 100 cm^2.

Studies of the WHIM, stellar accretion flows and coronal physics just three examples among a myriad of science cases for a high performance X-ray spectrometer. To advance the study of the energetic universe, there is a clear need for an instrument capable of making these measurements.

1.4 Goals for Present Research Program

I seek to lay the groundwork for the next generation of X-ray off-plane grating spectrometers which will bridge the performance 'gap' between currently operating instruments and the spectrometers capable of making the observations outlined above. As the aforementioned science case necessitates the improvement of systems-level performance, multiple limiting aspects of spectrometer design must be addressed simultaneously. The present work will solidify three major aspects of realizing a next-generation off-plane X-ray grating spectrometer:

1. **Grating manufacture:** As any grating spectrometer ultimately is an instrument translating the spatial distribution of X-ray photons into spectral information, the gratings in question must introduce minimal optical aberration. This is accomplished by the precision shaping of the ultrafine (< 1 μm) structures which constitute the grating grooves.

2. **Optical layout:** Astrophysical missions are subject to 'hard' design constraints imposed by the orbital/suborbital vehicle, environmental conditions and budgetary concerns. In addition, X-ray spectrometers are complex optical

systems in which there are many coupled variables. A suitable optical design must optimize instrument performance within this degenerate variable space while paying heed to given 'hard' boundaries of the specific mission in question.

3. **Optical alignment:** At X-ray grazing incidence, stacking or 'nesting' hundreds of optics next to each other is essential to obtaining large collecting areas. However, these optics must be co-aligned to within minute fractions of a degree in order to not compromise the system-level performance of the instrument. Ensuring that the spectrometer optics are co-aligned and stay so after bonding and launch is a major challenge for future spectrometers.

I will address each of these areas systematically through the design, manufacture and assembly of a grating module for an astronomical mission: Off-Plane Grating Rocket Experiment (OGRE). OGRE is a suborbital rocket whose payload is an off-plane X-ray reflection grating spectrometer capable of achieving resolutions of $>$ 1500 and effective areas of $>$ 40 cm^2 over the entire soft X-ray bandpass (0.3 – 1.5 keV). OGRE will have approximately 300 seconds of observing time on Capella, an X-ray bright, stellar binary source located in the constellation Auriga. OGRE is slated for launch in 2018 from Poker Flat Research Range near Fairbanks, Alaska.

Chapter 2 provides an overview of the steps already taken towards realizing a completed and flight-ready grating module, while Chapter 3 discusses the scope and methods of thesis work in detail. The products resulting from this research are summarized in 3.6, and Chapter 4 presents a timeline for achieving these goals.

Chapter 2

Current Status of Present Research Program

Considerable progress towards realizing a next-generation spectrometer has been made in recent years. Specifically, I have developed a new method of fabricating off-plane gratings with common microfabrication techniques. The process allows the gratings to be customized for any given mission architecture, and hence realize their maximal potential in a variety of configurations. These customized gratings have also been X-ray tested at multiple stages of manufacture, verifying their performance in the soft X-ray. Finally, a preliminary design for the OGRE spectrometer has been completed via full-system raytracing. The resulting instrument performance has been calculated and meets the performance standards set for the mission.

2.1 Off-Plane Grating Manufacture

2.1.1 Process Requirements

The off-plane diffraction geometry (Figure 1.2) requires a customized grating in order to achieve optimal resolution and diffraction efficiency. First, the grating grooves must be radially ruled in order to realize high diffraction efficiency (Cash, 1983). This radial fanning of the grooves matches the convergence of the incident beam and ensures the inherent linespread function of the telescope is not aberrated, which would result in poor resolution. To see the need for a radially ruled groove pattern, consider a grating placed in a converging beam. The relative angle between the grooves and the incident X-rays will vary over the face of the grating for a parallel groove pattern. This relative angle (α in Figure 1.2) enters into the grating equation

(Eq. 1.1), such that the variation in this relative angle would result in a variation of β for a given wavelength and yield a broad spectral line. However, if the grating is radially ruled, the relative angle between the X-rays and the grooves is kept constant over the grating face, dispersing photons of the same wavelength to the same location on the diffraction arc regardless of incidence location.

The facets of the grating grooves must also be specially shaped to realize the off-plane blaze condition and maximize diffraction efficiency. By sculpting a triangular groove profile, light is preferrentially diffracted to either positive or negative orders. This phenomenon can be exploited to maximize diffraction efficiency for a given physical extent of the diffraction arc, equivalent to a given range in wavelength space. At the systems-level, this effect can be used to increase a spectrometer's effective area near particular spectral lines of interest. Like the in-plane diffraction geometry, the off-plane configuration has a 'Littrow' configuration in which the intensity of a particular order is maximized. In this configuration, $\alpha = \beta = \theta$, where θ is the groove facet angle; Figure 1.2 shows a grating in the Littrow configuration for light that would be dispersed to β.

In order to diffract at X-ray wavelengths, the groove densities must be large compared to optical diffraction gratings. Typical groove densities for off-plane gratings range from 4,000-10,000 grooves/mm (periods: 250–100 nm). In addition, the grating must be manufactured over areas large enough to contribute efficient collecting area for a spectrometer. In practice, this means patterning areas on the order of 100 cm^2 (100 mm per side for a square grating). Finally, the resulting gratings need to exceed the figure requirements for the optical system in question. Any grating substrate deviations from flat translate into local variations of grating orientation. These local variations compromise the reflection off of the grating, blurring the line-spread function of diffracted orders at the focal plane and compromising the overall performance of the spectrometer. Based on the optical configuration of the spectrometer being considered, the diffraction equations can be translated into a set of figure requirements which limit the aberration to a tolerable[1] level (Allured and McEntaffer, 2013). Hence, at the end of manufacture, the flight gratings must meet the derived figure requirements. To summarize, the gratings for a high performance spectrometer must have:

1. Radially fanned grating grooves

2. Angled 'blazed' facets

[1]What constitutes 'tolerable' is in turn based on the science requirements of the spectroscopy mission.

3. High groove densities
4. Large patterned areas
5. Optical figure quality

2.1.2 Off-Plane Grating Microfabrication Procedure

Off-plane gratings that meet all of these requirements can be manufactured via a nine-step microfabrication process outlined in Figure 2.1. First, a silicon wafer is coated with two process layers: a silicon nitride hardmask and nanoimprint resist (Step #1). These layers are deposited over the thin ($\sim$5-10 Å) native silicon dioxide layer present on the substrate. Next, a nanoimprint mold with the desired groove distribution is prepared for use (Step #2). The mold is a grating which has the desired groove density, been radially ruled to the correct convergence angle, and is the same size as the final flight gratings. However, the mold has a laminar (i.e. 'square wave') groove profile and lacks the figure quality required for flight gratings. The mold manufacture processing is described in detail in McEntaffer et al. (2013). Before use, molds must be coated with a release chemical to ease the separation of the mold from the substrate. Failure to do so results in damage to the substrate and/or the transferred pattern upon mold release. Nanoimprint lithography (NIL) is then used to transfer the mold pattern to the substrate (Step #3). In thermal nanoimprint lithography (T-NIL), the mold is brought into contact with the resist layer. The substrate is then heated, bringing the nanoimprint resist to a temperature above its glass transition temperature. The mold is pressed into the liquid resist using a pressurized air bladder. The substrate is then rapidly cooled and the mold separated, thus transferring the mold pattern in negative into the 'cast' resist. A subsequent reactive ion etch (RIE) step (Step #4) transfers the imprinted pattern through the residual resist and the silicon nitride layer down to the silicon substrate. An sonication step (Step #5) in acetone removes any remaining nanoimprint resist, leaving strips of silicon nitride which match the mold grating pattern in negative.

A dip in buffered HF (Step #6) removes the layer of native silicon dioxide, exposing the bare silicon wafer. The sample is then transferred to a chemical bath for an anisotropic KOH wet etch (Step #7) which will sculpt the triangular shape of the groove facets. In crystalline silicon, the KOH etch rate in the <111> direction is orders of magnitude slower than in other crystallographic directions. Using an etch mask, this anisotropy can be exploited to preferrentially etch along the (111)

planes and form angled grooves whose facets are the bounding (111) planes of the etch mask.

The facet angle of the grating grooves can be tuned by selecting silicon wafers for which the angle between the <111> direction and the wafer normal is equal to the desired blaze angle. Off-the-shelf silicon wafers are manufactured in a variety of orientations, which, by definition, have a different crystallographic orientation which defines their wafer normal. The normal of a <100> wafer, for instance, is the <100> direction of a silicon lattice. For each wafer orientation, the relative angle between the <111> direction is different. Hence, after processing via the described method, these different wafer orientations yield gratings of different blaze angles. The resulting facet angles for a number of common silicon wafer crystallographic orientations are given in Table 2.1. Silicon foundaries are often also capable of dicing silicon ingots 'off-axis,' resulting in a wafer normal that is slightly rotated ($< 10°$) from the nominal ingot orientation. Through off-axis cutting of wafers with different crystallographic orientations, it is possible to obtain any blaze angle that might be desired for a spectrometer.

Wafer Orientation	Blaze Angle
<111>	0°
<211>	22.4°
<311>	29.5°
<511>	38.9°
<711>	43.3°
<100>	54.7°

Table 2.1: Facet angles achievable using different crystallographic orientations of silicon wafers.

In the KOH wet etching step, the grating pattern in the silicon nitride serves as an etch mask; where bare silicon is exposed between silicon nitride strips, substrate material is removed until reaching a (111) plane intersecting the bounding silicon nitride strip, at which point the etch (effectively) stops. Thus, the resulting sample has the original groove density and radial profile of the imprint mold but blazed, triangular facets. The silicon nitride mask is next removed by a soak in HF (Step #8) which chemically dissolves the silicon nitride without affecting the silicon substrate.

At this point, the only requirement not met by the existent sample is optical figure quality. Silicon wafers have global flatness specifications that are outside the figure qualities needed for off-plane gratings. Fused silica substrates, on the other hand,

are optically flat to high precision and are relatively cheap. By imprinting the blazed silicon grating into resist on a fused silica substrate (Step #9), the radially ruled, blazed grating profile can be replicated on a surface meeting the required figure. As a secondary benefit, a second imprint makes the production of flight gratings a more cost- and time-effective process, as the same silicon grating can be used for multiple imprints, thus boosting process yield. As the resist on the fused silica will ultimately contain the desired grating pattern, it must be mechanically durable for flight and able to withstand the deposition of an X-ray reflective layer (Step #10) over top of the resist. Energetic ions impacting T-NIL resist during thin film deposition can oblate the imprinted pattern. In addition, these ions also deposit thermal energy into the substrate, which can heat the thermal resist and alter the cured pattern. T-NIL is also temporally unstable, losing its fidelity to the imprinted profile over time. UV nanoimprint lithography (UV-NIL), on the other hand, uses a liquid polymer which cures after exposure to UV light and has significantly better mechanical and thermal stability, making it a better candidate for the second, final imprint. The deposition of a thin reflecting layer, such as gold, platinum, or iridium, concludes the fabrication process and yields an off-plane grating of flight quality.

2.1.3 Grating Production at Iowa

Using the described process, I have successfully made prototype off-plane gratings similar to those that would be used in a next-generation spectrometer. I obtained three types of wafers which yield different blaze angles: a <111> wafer cut 10° off-axis (10° facet angle), a <311> wafer (29.5° facet angle), and a <100> wafer (54.7° facet angle). These were processed through the HF soak step (Step #8 of Figure 3) at the UIMF, then sent on to Nanonex Corporation for the remaining imprint and reflective coating steps.

The grating mold employed for the imprint measures 32 mm × 25 mm, matches the convergence of a telescope with an 8.4 m focal length, has a 50% duty cycle, and has a groove density averaging[2] 6033 gr/mm. The grating template has been extensively tested in X-rays and has demonstrated absolute diffraction efficiencies of $> 40\%$ (McEntaffer et al., 2013) and resolving powers > 3000 (McEntaffer, 2015).

Figure 2.2 shows Scanning Electron Microscope micrographs (SEMs) of several in-process sample gratings. The current device 'recipe' for off-plane gratings with reference to the tools available at the University of Iowa Microfabrication Facility

[2]Note that due to radial ruling of the grating, the groove density changes along the optical axis of the grating. The number given here is the nominal groove density at the physical center of the grating pattern.

(UIMF) is explicitly described in Appendix A. While this method has been successfully used to fabricate blazed gratings, there are several drawbacks to the current execution of the manufacturing process which I briefly elaborate upon here.

For Step #1, each process wafer is coated with a 45 nm thick layer of silicon nitride using a reactive ion sputtering process performed by a Intlvac Nanochrome I Sputterer. In reactive ion sputtering, the process case is partially backfilled with a gas (in this case, nitrogen) which reacts with the ablated target material (in this case, silicon) on its way to the substrate. The result is a non-stoichiometric combination of the target and gas constituents as a thin film often referenced as SiN_x, where x represents the ratio of N to Si atoms incorporated in the thin film. Process wafers are then coated with approximately 95 nm of thermal nanoimprint resist via a spin coater. Ellipsometry measurements of each of these thin films demonstrates that the resist layer and the silicon nitride layer can vary by as much as ± 5 nm and ± 2 nm respectively over the extent of the imprinted area. This thickness variation has an impact on the uniformity of the silicon nitride etch mask after the RIE process, which, in turn, can result in variations of the groove profile over the grating. This issue must be addressed in order to yield consistent grating profiles (see Section 3.3).

As the (111) planes will ultimately form the grating groove facets, the grating mold must be correctly aligned to the crystallographic planes of the substrate during the T-NIL process (Step #3). For all crystallographic orientations mentioned in Table 2.1, the mold's grooves must be oriented along the <110> direction in order to stop the KOH wet etch at the (111) plane. Misalignments of the mold to the substrate result in 'undercutting,' in which other planes besides the slow-etching (111) are exposed to KOH, resulting in the removal of substrate material underneath the silicon nitride hardmask. Slight misalignments result in a zig-zag pattern of etch 'ledges' along the groove (Kendall, 1975), while a gross misalignment results in the total erosion of the grating pattern. The angular alignment tolerance of the mold can be directly translated into a spatial roughness scale, as the number (111) 'ledges' will increase as the angular misalignment increases. The grating mold is currently aligned to the <110> direction of the substrate by use of the alignment flats provided by the silicon foundry and is accurate to $\pm 0.5^\circ$. This angular tolerance is acceptable for prototyping, but better precision will be needed to produce gratings with low surface roughness.

After the patterning the resist with a grating template via T-NIL, the pattern must be transferred anisotropically through the resist and SiN_x layer to the silicon wafer. The reactive ion etch employed is a two-step process: one Ar/O_2 step for etching the resist layer and one CHF_3/O_2 step for etching the silicon nitride hardmask. T-NIL resist etches readily in O_2, meaning that removing material from the groove

sidewalls is difficult to prevent. The etch isotropy can be advantageous, however, as the Ar/O_2 etch can be used to narrow the resist plateaus, eventually resulting in a thinner silicon nitride 'tabs' for the KOH etch mask and an increased duty cycle of the blazed grating. The subsequent CHF_3/O_2 etch step for the silicon nitride layer is almost entirely anisotropic, but the (necessary) use of fluorine to remove the silicon nitride has the drawback that it will also etch into the underlying silicon substrate. The removal of substrate material results in a deeper groove trough; the removal of too much substrate material can lead to undercutting. Hence, non-uniformity in the silicon nitride layer can yield a grating which has a duty cycle which varies over the optical surface, or, worse, areas of the grating 'undercut' by the removal of too much substrate material.

Finally, the chemical resistance of the deposited SiN_x thin film to the buffered HF solution is uncertain. Metrology up to this point has shown that there is a high degree of variation resulting from similar (or even identical) buffered HF/KOH wet etch steps. Note the <111> 10° off-axis grating and the <311> grating in Figure 2.2 are both shown prior to the HF soak step which completely removes the silicon nitride hardmask, yet the remaining 'tabs' of SiN_x have very different appearances. Both of these substrates were exposed to identical buffered HF solutions for equal times.

2.2 Grating Performance Measurement

Of the three grating profiles produced via the off-plane grating microfabrication process, two have been tested in the X-ray to observe the resultant diffraction pattern. Both the <311> and the <111> 10° off-axis orientations were tested at the Max Planck Institute for Extraterrestrial Physics' X-ray test facility, PANTER (Figure 2.3). The PANTER facility consists of several X-ray fluorescence or monochromator sources which are housed at one end of a 122 m long, 1 m diameter vacuum chamber, forming a long 'beamline' over which source light can be collimated. At the opposite end, a 12 m long, 3.5 diameter instrument chamber is joined to the beamline and houses a customizable optical bench manueverable with vacuum stages. Imaging and energy-sensitive X-ray detectors are also housed in the instrument chamber. The entire vacuum apparatus is capable of reaching pressures $< 10^{-5}$ mbar. A schematic of our experimental set-up inside the instrument chamber is shown in Figure 2.4.

A custom silicon pore optic (SPO) mirror module was utilized to focus the incoming beam prior to incidence on the tested gratings. SPO mirror modules are formed from superpolished silicon plates that have been diced to form small ($\sim$1 mm) channels. These plates are then stacked atop one another to form 'pores' which

permit X-rays to pass through. By elastically deforming the plates around an inner mandrel and angling each subsequently stacked plate ('wedging'), the mirrors can be bent into a conical approximation of paraboloids or hyperboloids, thus enabling the construction of a Wolter-I type telescope. SPO stacks with 45 plates have achieved half energy widths[3] (HEW) of 15-17 arcseconds (Bavdaz et al., 2012). The SPO mirror module employed for this PANTER grating test was not a full Wolter-I, but instead an 14 plate stack consisting of only paraboloids. The SPO mirror module has a nominal radius of curvature of 450 mm, but after construction was measured to relax to 475 mm due to bending stress. The SPO has a focal length of $\sim$8.6 m at the finite conjugate distance of the source. The aberration caused by the slight mismatch of the SPO focal length to the convergence of the grating is small compared to the linespread function of the SPO.

An X-ray fluorescence source with a Mg target was used to measure the linespread functions of the SPO focus and the diffracted orders for both gratings. The gratings were aligned to the SPO focus and the rotation of the grating about its normal (the 'yaw' of the grating) zeroed. Each was then placed into the Littrow configuration for an incidence angle that enabled the sampling of multiple orders of Mg K (@ 1.254 keV) with the specified detector configuration. Functionally, reaching the Littrow configuration involves setting the pitch (or incidence angle) and the yaw of the grating: increasing the incidence angle serves to increase the radius of the arc, while increasing the yaw of the grating increases α. Recall that in the Littrow configuration, $\alpha = \beta = \theta$ (Figure 1.2). Through Eq. 1.1 and Eq. 1.2, it is possible to show that, in the Littrow configuration:

$$\lambda_{blaze} = \frac{2d \tan\gamma \tan\theta}{n}. \tag{2.1}$$

Manipulating the incidence angle of the grating thus enables the placement of a Mg K order at the ideal β. The grating is then placed into the Littrow configuration by giving it a yaw Ψ equal to:

$$\Psi = \sin^{-1}\left(\tan\gamma \tan\theta\right), \tag{2.2}$$

which can also be derived through geometric considerations.

The groove facets of the <311> grating were blazed towards positive orders and have an angle of $\theta = 29.5°$. While similar to the facet angles required for future spectrometers (Smith, 2014a), limitations on stage travel precluded the possibility of testing this grating at an incidence angle of $\gamma = 1.5°$, the incidence angle baselined

[3]The half energy width of an optic is the diameter of the circle enclosing half the focused power.

for most future grating instruments[4]. Thus, the <311> was tested at an incidence angle of 0.6°, which places the Mg Kα +2$^{\rm nd}$ order line near the location of highest diffraction efficiency.

As the <111> 10° off-axis grating has a shallow facet angle of $\theta = 10°$, a test incidence angle of $\gamma = 1.5°$ placed the ideal β in a location accessible to the focal plane detectors. However, this ideal β does not correspond to the wavelength of any line fluoresced by the Mg target, lying just between the position of -1st and -2nd order[5] of Mg Kα.

Spectral information is extracted from the data by collapsing the image in the vertical (cross-dispersion) direction. Any potential offset in the azimuthal position of the mirror relative to the grating normal (an effective 'roll' of the grating, see Figure 3.1) will yield a rotated linespread function, broadening the observed line in wavelength space. This effect can be deconvolved from the data by fitting a line to the linespread function of the 0$^{\rm th}$ order image and deriving a rotation from the best-fit slope. This same rotation is then applied to the images of all diffracted orders for that grating.

Rotated images of diffracted orders from the <311> grating are shown in Figure 2.5, while those from the <111> 10° off-axis grating are shown in Figure 2.6. The collapsed linespread functions are fit with a Gaussian line profile. The data and fits are normalized by equating the amplitudes of the Gaussian fits. The lines can then be compared side-by-side to determine the change in the linespread function from the spectral focus to the diffracted spot (Figure 2.7 for the <311> grating, Figure 2.8 for the <111> 10° off-axis grating). The errors on the FWHM in Figures 2.7 and Figure 2.8 are derived from the Gaussian fits to the data and are 1σ errors.

The focus quality of the SPO in the cross-dispersion direction ($\sim$3.9") is too poor to support measurements of high resolving power from these gratings. Nevertheless, the measurements show that the linespread function observed in zero order is largely preserved even at large β, thus precluding grating induced aberration at this focus quality. Figs. 2.7 and 2.8 show that the spectular reflection from both the <311> and the <111> 10° off-axis grating is identical to the SPO focus to within 3σ. Furthermore, the linespread functions of all diffracted orders are statistically indistinguishable from to their zero order counterparts at 3σ significance, with the notable exception of two lines at high dispersion locations: the <111> 10° -3$^{\rm rd}$ order

[4]Testing the <311> grating at an incidence angle of $\gamma = 1.5°$ required 250 mm of stage travel from zero order; the PANTER test configuration used for this test supported approximately 100 mm in the direction of the <311> blaze.

[5]Note that the groove facets for the <111> 10° were blazed towards negative orders, hence the change in order 'sign' from the <311> diffracted orders to the <111> 10° off-axis diffracted orders.

line (3.2σ) and the <311>+2^{nd} order line (3.5σ).

There are known systematic errors which contribute to the broadening of the linespread function in the spectral direction at high dispersion locations. Optical path length differences due to the physical width of the grating and the curvature of the focal plane are expected to be the dominant broadening effects for this optical configuration, though other errors (e.g. the figure quality of the optic, the mismatch of the radial profile to the convergence of the telescope, etc.) are expected to contribute. These errors likely account for the systematic increase of the FWHM from zero order to the diffracted orders and contribute to the broadening of the aforementioned lines outside the 3σ significance threshold. Modeling the optical system via raytracing will clarify which broadening effects are expected to dominate. Given adequate statistics in the observed lines, raytracing studies may also enable the deconvolution of these errors from the observed linespread function in order to establish an upper limit on any grating-induced aberration, an important result for gratings fabricated using this technique.

The PANTER measurements also empirically verify a significant premise of our microfabrication studies: sculpting the groove profile through the microfabrication process can be used to change the efficiency response at a specified energy. Diffraction efficiency measurements show that at 1.25 keV (approximately the energy of Mg Kα), the efficiency of the grating mold in second order is nearly zero, owing to an interference pattern between the groove trough and groove plateau (McEntaffer et al. (2013)). The <311> grating, identical to the mold save in the groove profile, is not only demonstrated to have a non-zero response at Mg Kα +2^{nd} order, but this line is in fact 25% brighter than the +1st Mg K order line when operated in the Littrow configuration. Rigorous efficiency measurements of a blazed grating over a wide range of orders and energies should be made to quantitatively exhibit this finding; nevertheless, these PANTER measurements provide strong empirical evidence that customizing the groove profiles of off-plane gratings can improve the effective area of grating spectrometers at wavelengths of interest. Analysis of these measurements is ongoing, and will conclude in a publication in Spring 2015 (see 3.6).

2.3 Optical Design of the OGRE Spectrometer

As discussed in Section 1.4, my thesis work also includes the optical design of the X-ray grating spectrometer onboard OGRE. OGRE will be the first astronomical mission to fly customized off-plane gratings made from the microfabrication technique described in Subsection 2.1.2. OGRE will also leverage a new X-ray mirror manufacturing technique developed at Goddard Space Flight Center (GSFC), and

use a specialized charge-coupled device (CCD) detector to achieve unprecedented performance in the soft X-ray bandpass. Thus, OGRE represents an important milestone towards a future X-ray observatory, realizing spectral performance beyond the capabilities of *Chandra* and *XMM-Newton* in an easily scalable, cost-efficient means.

OGRE will use a traditional Wolter-I style telescope consisting of thin single-crystal silicon mirrors to achieve an optical focus quality ~ 2" in the dispersion direction. Such a tight linespread function enables high resolutions even within the bounds of a suborbital rocket envelope. The manufacturing process for these mirrors (Zhang et al., 2014) begins with a block of cut silicon which has been chemically etched to remove any surface damage. Next, the desired optical shape is cut and the surface polished using a commercially available polishing technique. The mirror figure can be tested and qualified at this point, allowing for the possibility of an iterative process to improve the mirrors focusing power over several polishing cycles. When the required figure is achieved, the optical surface is removed by slicing a thin face-sheet from the silicon block. This eliminates the excess silicon and serves to lightweight the mirrors. However, the cutting process creates surface damage on the back (convex) side of the mirror, which imposes new stress and distorts the figure. A chemical etch and/or annealing can remove this damage and should restore the original figure.

In addition to employing these cutting-edge mirrors, OGRE will also make use of EM-CCDs at the focal plane, which have seen limited space-flight application up to this point but have immense promise as X-ray detectors (Tutt et al., 2014). At the low end of the soft X-ray bandpass (0.3 – 0.6 keV), the effective area of grating spectrometers is mainly limited by detector effects. For one, X-ray photons have a high probability of registering as 'split events,' or spreading the liberated electrons over multiple pixels in a CCD. This serves to reduce the signal-to-noise ratio in a given pixel. For soft X-ray photons, this split effect can dilute the signal below the noise threshold, resulting in lost events. EM-CCDs have several advantages in detecting these low energy X-ray photons. EM-CCDs differ in that the signal passes through an electron multiplication register before chip readout, which serves to amplify the input signal. As amplification occurs before the charge is output, readout noise is suppressed, and the overall signal-to-noise ratio of the device is improved. Thus, even soft split X-ray events can be amplified above the noise threshold, greatly increasing the detectability of low energy photons and helping to maintain high effective areas near the soft energy cut-off.

These two critical technologies have been more throroughly discussed elsewhere (thin, single-crystal mirrors: Zhang et al. (2014) and references therein, EM-CCDs

for X-ray spectroscopy: Tutt et al. (2014)), and a broad overview of the OGRE mission has already been provided (DeRoo et al., 2013). Creating an optical configuration which maximizes the performance of this unique spectrometer, however, is a non-trivial challenge that merits its own discussion. Firstly, realizing high performance within the payload envelope of a sounding rocket is difficult owing to the relative speed[6] of the optical system. X-ray optical systems typically have focal lengths on the order of 8 – 10 m – *Chandra* and *XMM-Newton*, for example, have focal lengths of 10.0 m and 7.5 m respectively. On the other hand, in a sounding rocket, flight stability dictates an instrumental payload length less than 4.5 m. This impacts the distance between the grating assembly and the focal plane L, resulting in less dispersion (Eq. 1.2), which can ultimately impact resolution. Secondly, the limited payload diameter also impacts the radial extent of the mirror assembly. As the geometric area of the mirror assembly provides an upper limit on the spectrometer's effective area, achieving high effective areas in a rocket envelope is rarely as simple as adding additional mirrors. Finally, the optical assembly must hold within alignment tolerances over launch, which has greater accelerations than most observatory launches.

To design an optical assembly meeting the OGRE performance requirements within these instrumental bounds, a series of custom Python packages called *SpectDesign* was written. *SpectDesign* requires a set of input parameters which dictate important instrumental constraints, such as the focal length and radial extent of the mirror assembly, grating incidence angle, groove density, etc. and solves for the number of optics (paraboloids, hyperboloids, and gratings) as well as individual positions of each optic required to build a given grating spectrometer. The instrumental configuration can then be exported to a text file or to Solidworks for CAD rendering. The response of the instrumental configuration to source photons can also be simulated with *SpectDesign* via 'raytrace,' in which individual photons are propagated through an optical configuration geometrically. *SpectDesign* also includes scripts which incorporate phenomenological effects like scattering and diffraction, making it possible to simulate the spectral locations of diffracted spots as well as the resolutions achieved by the instrument at a given wavelength. Finally, through the use of libraries containing the X-ray reflectivities of different materials at various incidence angles, the effective area of the configuration can be calculated. Even if raytraced iteratively to build up a statistically significant ($N \sim 100$) number of predicted instru-

[6]Formally, the focal length of the telescope divided by the aperture. For our purposes, take this to be the ratio of the focal length to the inner radius of Wolter-I mirrors. A 'fast' telescope has a small ratio, requiring a larger angle of convergence for the light to reach the focus. Note that even 'fast' X-ray systems are 'slow' by optical telescope standards.

mental responses, the total time taken for each configuration calculation is less than fifteen minutes, making it possible to iteratively explore the complex design space and obtain quantitative comparisons between different instrumental configurations.

SpectDesign positions and orients the gratings based on a mathematical construction known as the Rowland circle. The Rowland formalism was originally derived for concave optical gratings and is a geometric construction ensuring that diffracted orders appear at the same spatial position at the focal plane, despite incidence at different azimuths along the concave surface (Born and Wolf, 1999). In the X-ray, the Rowland formalism is coopted into grazing incidence by using an array of gratings 'fanned' along the azimuthal extent of the Rowland circle. By the geometry of the Rowland formalism, the ideal focal plane is also curved, lying along a 3-dimensional toroidal surface[7] defined by rotating the Rowland circle around the axis defined by the telescope focus and the spectrometer focus (the zero order position). Gratings positioned on the Rowland circle have been successfully used for the *XMM-Newton* Reflection Grating Spectrometer (den Herder et al. (2001)), and are the baseline optical configuration for any off-plane grating spectrometer. Figure 2.9 shows the *XMM-Newton* and the OGRE Rowland circle designs.

Employing the Rowland circle to position the gratings for OGRE, however, illustrated a new issue for fast spectrometers. The Rowland formalism ensures that orders are diffracted towards the same position on the focal plane; however, it makes no attempt to account for the difference in optical path length between reaching the telescope focus and the spectral focus. Thus, diffracted light from different incidence locations on the grating array may be intra- or extra- focal at the focal plane defined by the Rowland formalism, which then yields an aberration in the linespread function.

The effect of this aberration can be seen in Figure 2.10, which shows the resolution obtained via *SpectDesign* raytracing for a single OGRE module (focal length $z_0 = 3500$ mm, inner mirror radius $R_0 = 300$ mm). The radial extent of the single module is then increased in increments of 25 mm and the resulting resolution calculated via raytrace. The resolution is measured at 37.5 Å, which at the focal plane is at the same location as third order 12.5 Å, the approximate wavelength of a suite of bright Fe lines which will be observed by OGRE. Obviously, the azimuthal extent of the grating array must grow as the radial extent of the Wolter-I telescope increases in order to continue to intercept all of the converging beam. However, the outermost gratings, i.e. the positions with the greatest azimuthal difference from the center grating, have the greatest path length difference from telescope to spectral focus. Hence, there is a direct trade-off between resolution and effective area: as the effective area

[7] sometimes known as the Rowland torus

grows by increasing the geometrical area of the telescope, the optical path length difference also increases and degrades the instrumental resolution. This problem with the Rowland circle placement is exacerbated by the fast OGRE telescope - the relatively short focal length requires a more rapidly converging beam, which in turn yields a less focused beam when sampled intra-/extra-focally.

Thankfully, realizing high resolutions and effective areas using fast X-ray telescopes can still be accomplished by using a new, multi-module optical configuration. Figure 2.10 shows that even at short focal lengths, reasonable radial mirror extents ($\sim$100 mm) can still achieve $R > 2000$. Defining an optical module as one coupled mirror (P/H) and grating set, it is possible to achieve greater effective areas by utilitzing multiple modules (each defined by a separate Rowland circle) and co-aligning the modules. In this way, the grating arrays within each module are limited to the regime where the optical path length difference is not severe enough to create an unacceptable aberration, and the path length differences between modules are controlled via adjusting either the focal length of the mirrors or the mirror module's position along the optical axis.

The constraints needed to realize a multi-module Rowland circle design meeting the necessary resolution and effective area requirements, were scripted and added to *SpectDesign*, enabling iterative raytraces with adjustable module parameters. This scripting has also enabled the realization of a preliminary OGRE optical design which acheives resolutions of > 2000 over the soft X-ray bandpass while maintaining effective areas of > 40 cm^2. Figure 2.11 shows the *SpectDesign* generated mathematical layout and the mirror layout realized in CAD. The expected effective areas from such an instrument is shown in Figure 2.12.

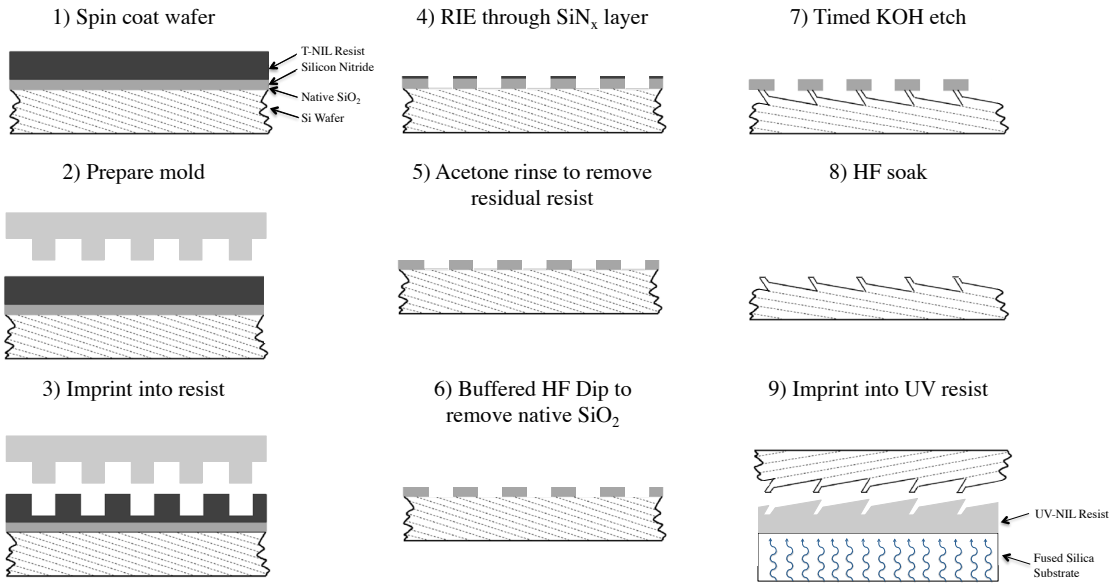

Figure 2.1: Procedure for fabricating off-plane gratings.

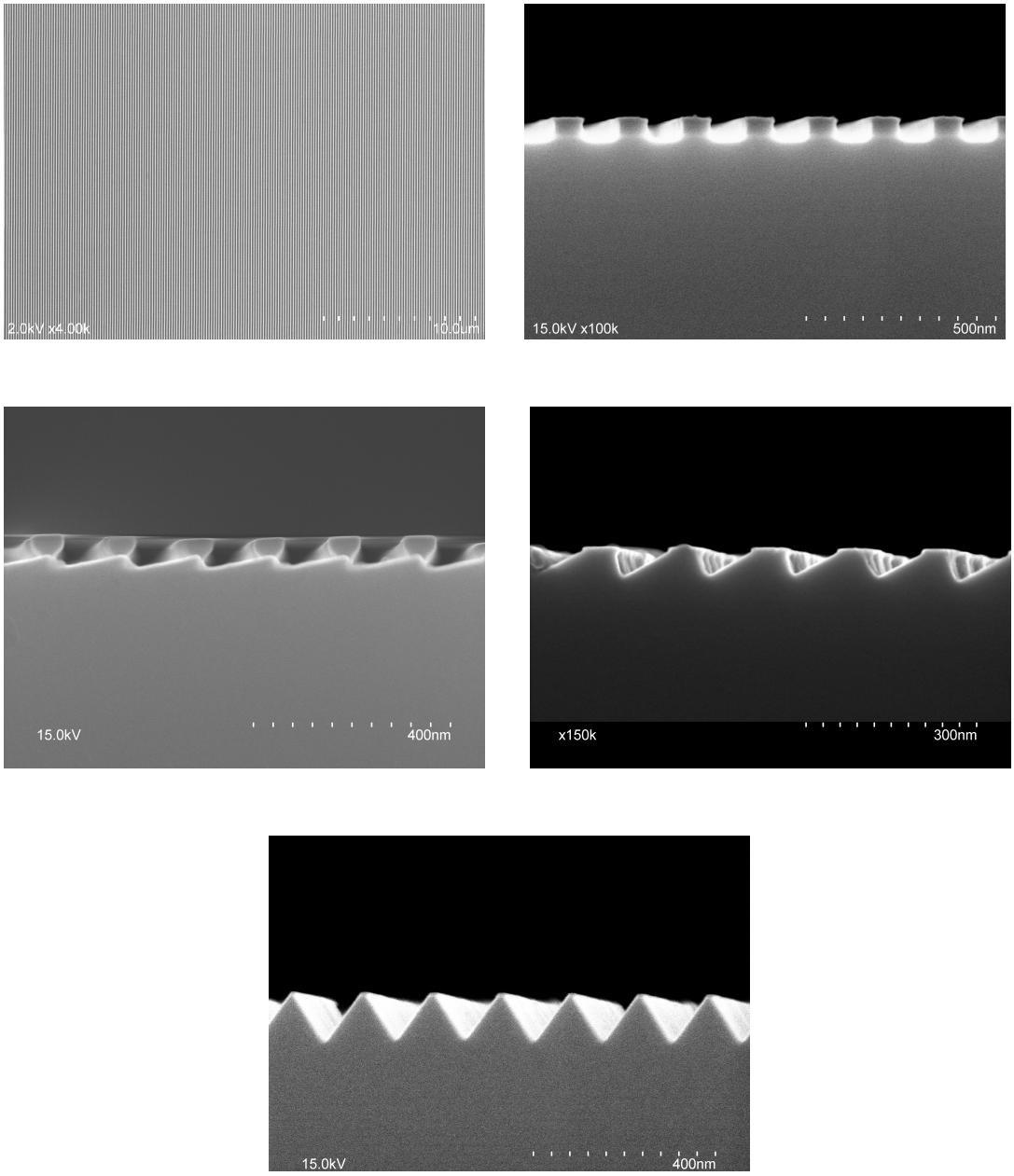

Figure 2.2: (*Top Left*) In-process grating, viewed from the surface normal. The sample has been through RIE and acetone sonication steps (Step #5) forming the silicon nitride hardmask. (*Top Right*) The silicon nitride hardmask, viewed 'edge-on,' or along the grating grooves. (*Middle Left*) A <111> 10° off-axis silicon wafer through the KOH wet etch step (Step #7) viewed 'edge-on.' (*Middle Right*) A <311> silicon wafer also through the KOH wet etch step viewed 'edge-on.' (*Bottom Center*) A <100> silicon wafer processed through Step #8, the HF soak step.

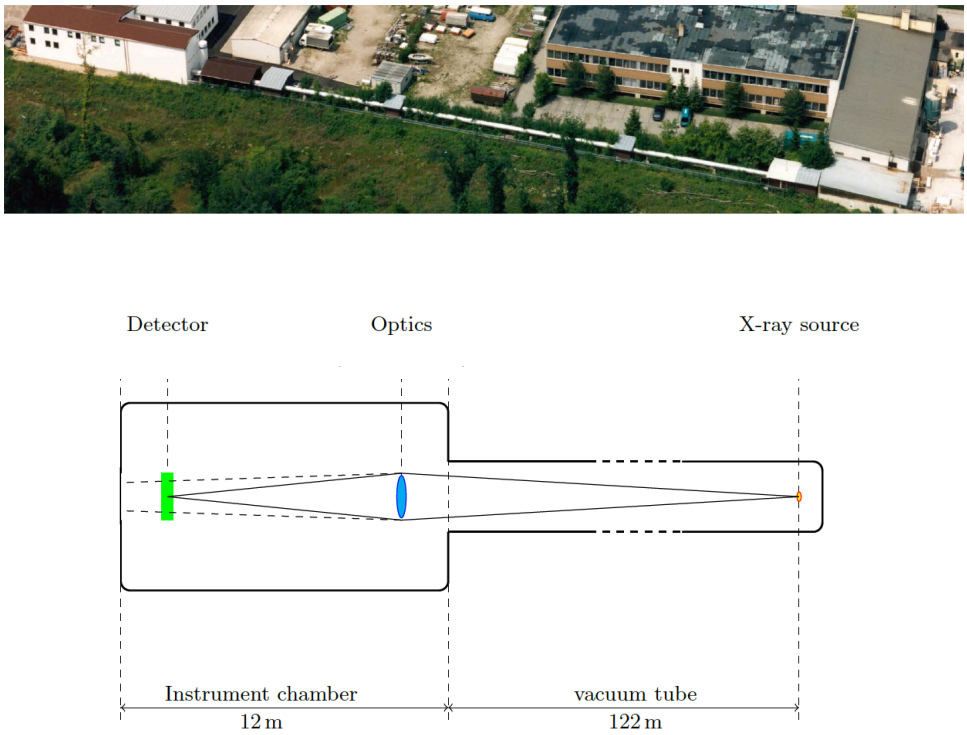

Figure 2.3: (*Top*) The PANTER X-ray test facility from the air. The X-ray source is housed on the right side of the image, while the instrument chamber is housed in the white building at the left edge of the picture. (*Bottom*) A diagram showing a generalized PANTER experiment.

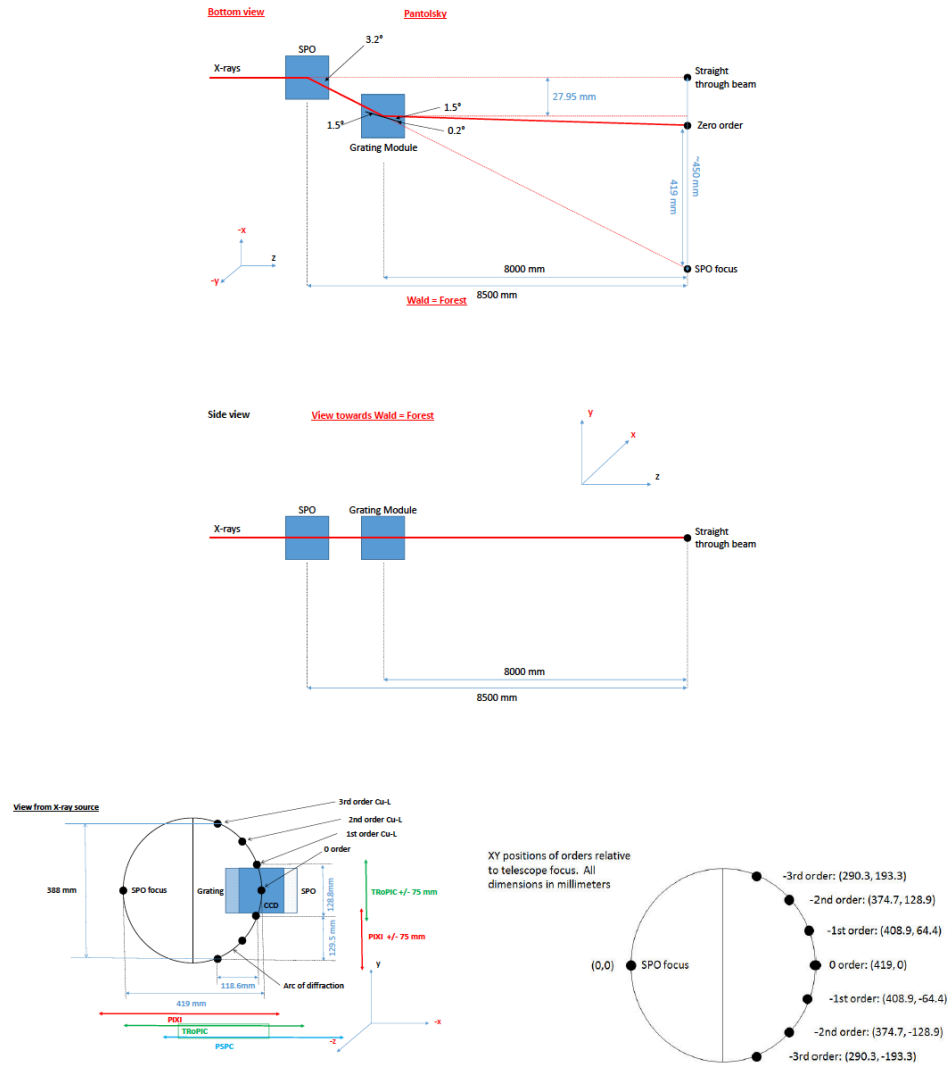

Figure 2.4: Diagram of the off-plane grating test setup in the instrument chamber at PANTER. An SPO mirror module intercepts the incoming light from the X-ray source and focuses it at a point displaced in the $+x$ direction (termed 'Wald' at PANTER). The gratings then intercept this focused beam, reflecting it towards -x ('Pantolsky'). Dispersion occurs along the y axis. By way of an example, the diffraction pattern of Cu-L (@ 0.928 keV) is shown at the bottom.

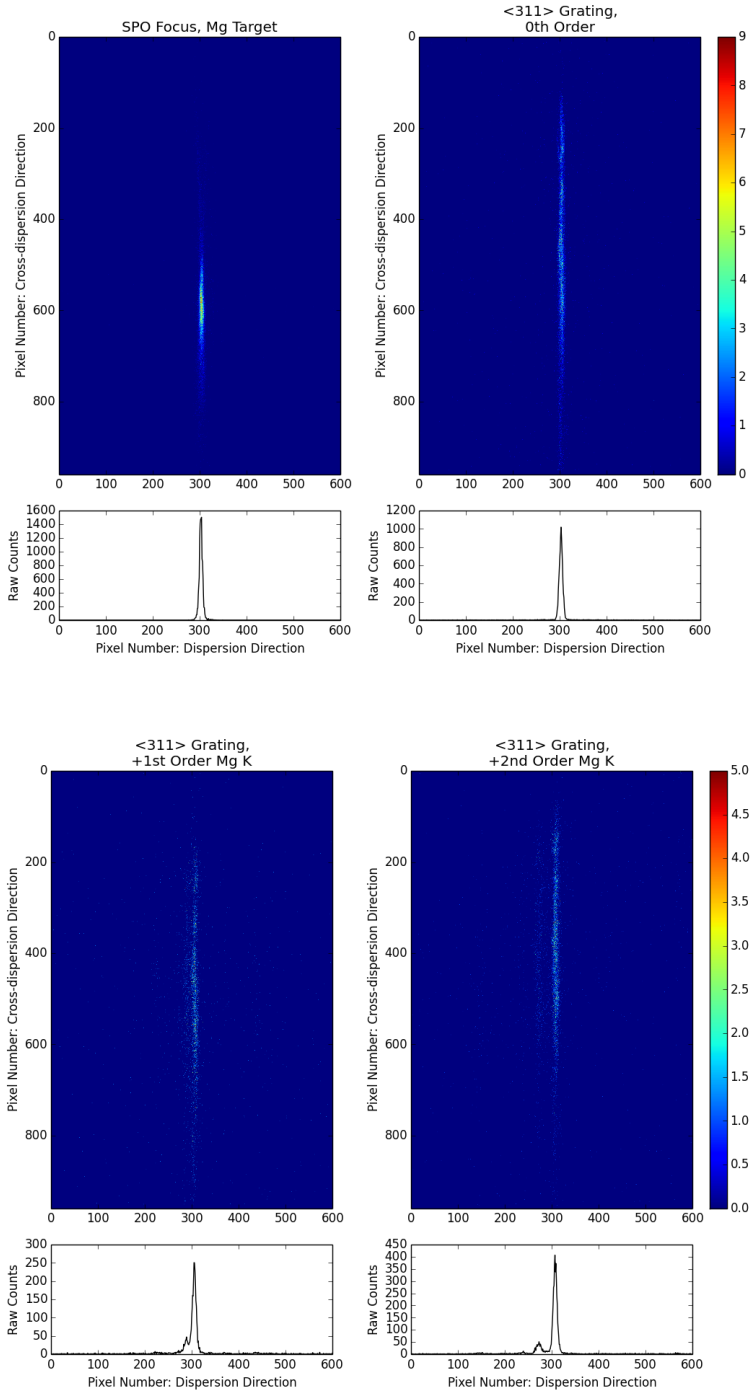

Figure 2.5: CCD measurements of the SPO focus, the spectral focus (0^{th} order), and the diffracted spots from the <311> grating. All of these images were taken with the TRoPIC camera.

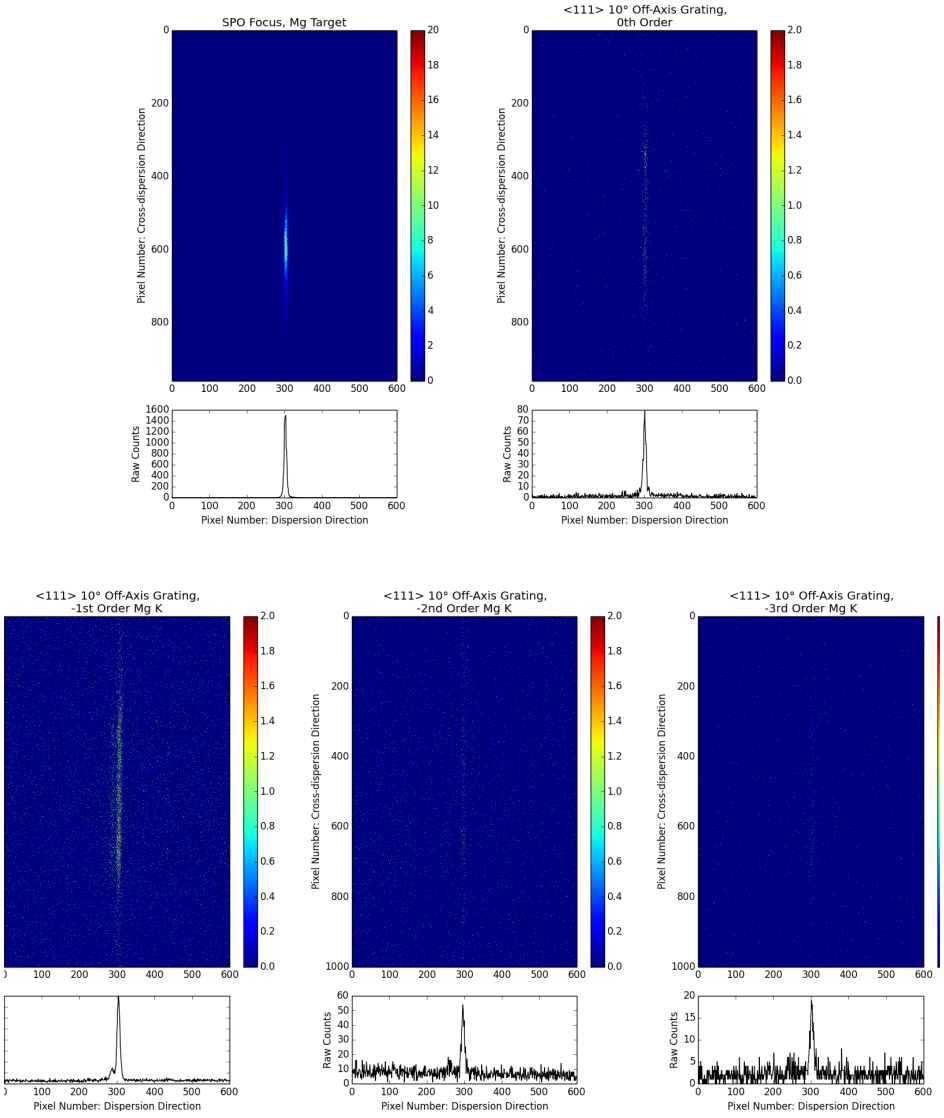

Figure 2.6: CCD measurements of the SPO focus, the spectral focus (0^{th} order), and the diffracted spots from the <111> grating. Note that the SPO focus measurement is identical to that of Figure 2.5. The SPO focus and the spectral focus were sampled using the TRoPIC camera, while the diffracted orders were imaged with the PIXI camera.

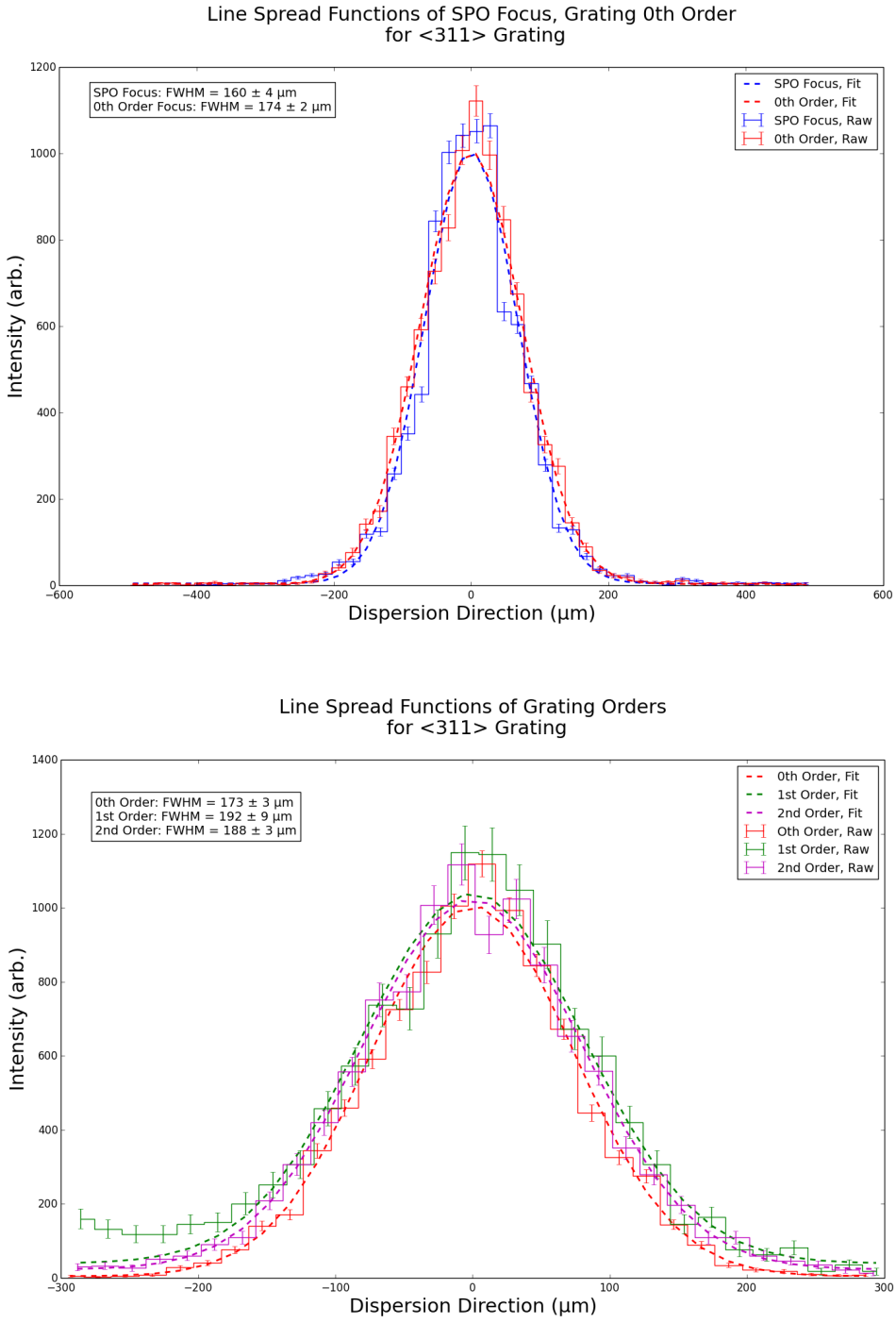

Figure 2.7: Side-by-side comparisons of the SPO focus and spectral focus (*Top*) and the spectral focus and diffracted orders (*Bottom*) for the <311> grating.

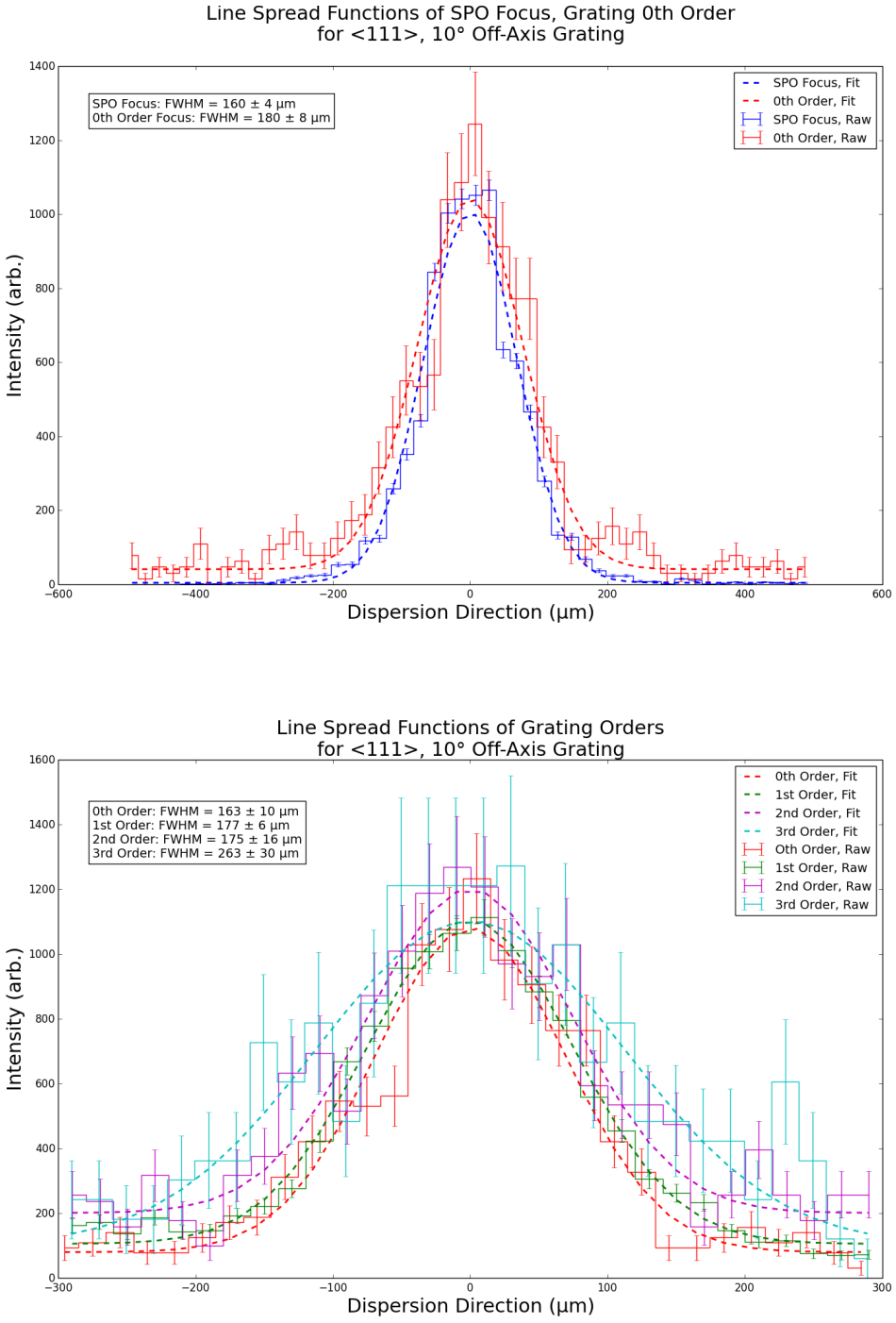

Figure 2.8: Side-by-side comparisons of the SPO focus and spectral focus (*Top*) and the spectral focus and diffracted orders (*Bottom*) for the <111> 10° off-axis grating. Note that for Mg K -3rd order, there are a low number of events (N < 100) contributing to the large fit errors.

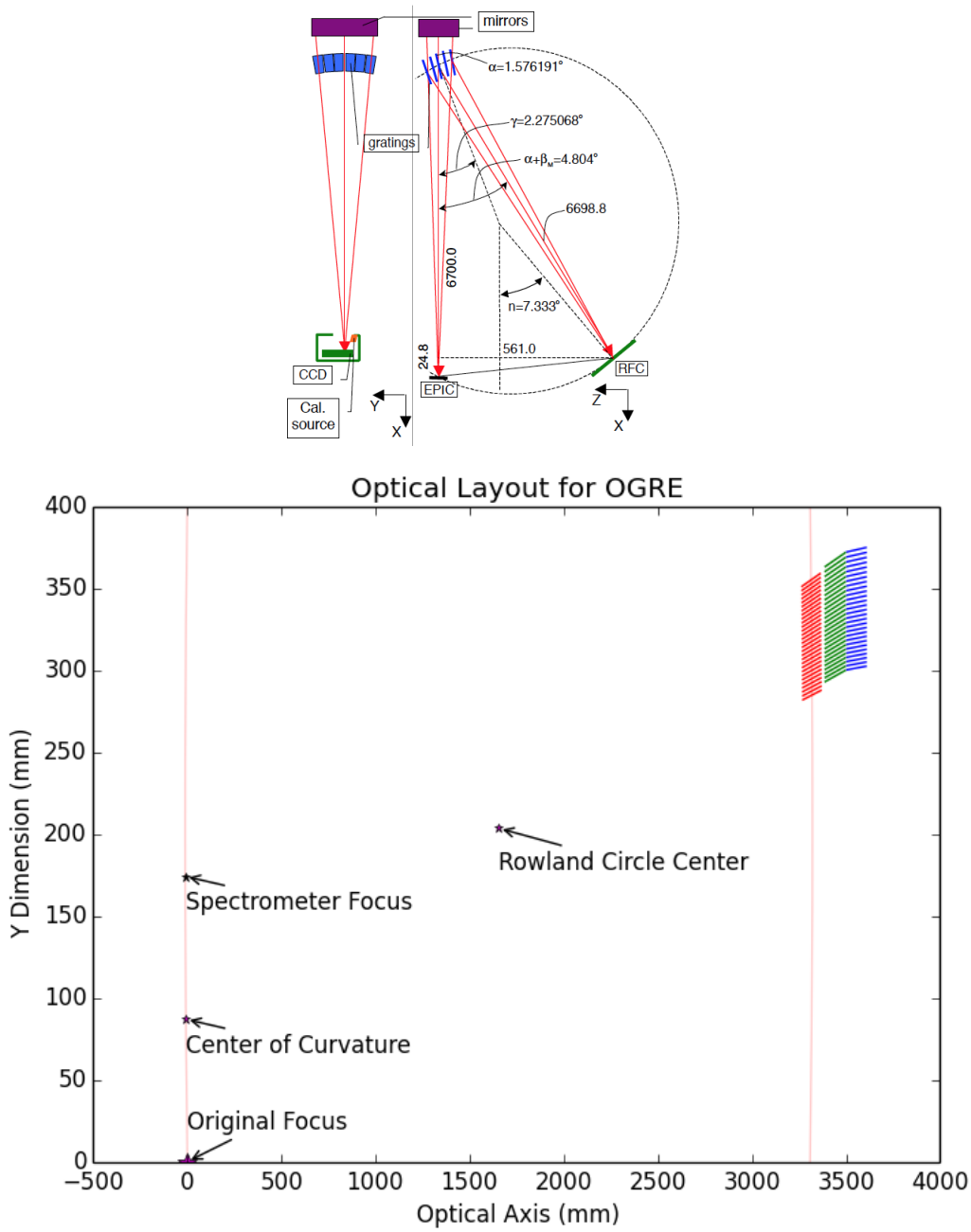

Figure 2.9: (*Top*) The Rowland circle design for *XMM-Newton* (den Herder et al., 2001, Fig. 1). (*Bottom*) An example of a similar Rowland circle design for OGRE, as output by *SpectDesign*. Note that the OGRE design is not to scale. The paraboloid mirrors are shown in blue, hyperboloids in green, and gratings in red, while the dashed red line outlines the fictional Rowland circle.

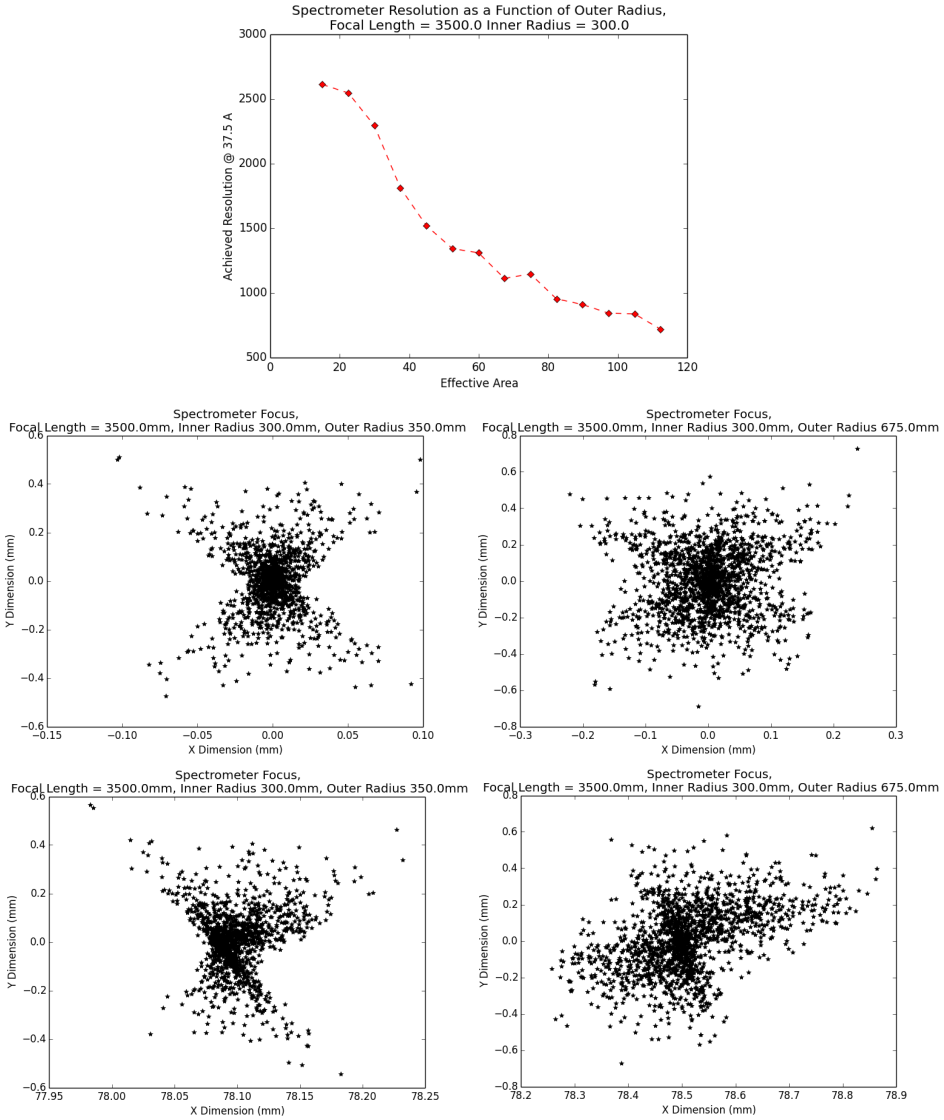

Figure 2.10: (*Top*) A plot of spectrometer resolution as a function of the outer radius R_{max} of the telescope given a set inner radius of 300 mm. The linespread function of the spectral focus (0^{th} order, *Left Middle*) and the diffracted spot (*Left Bottom*) for a telescope with $R_{max} = 350$ mm. Compare the linespread function to that of a telescope with $R_{max} = 650$ mm. (0^{th} order, *Right Middle*, diffracted spot (*Right Bottom*).

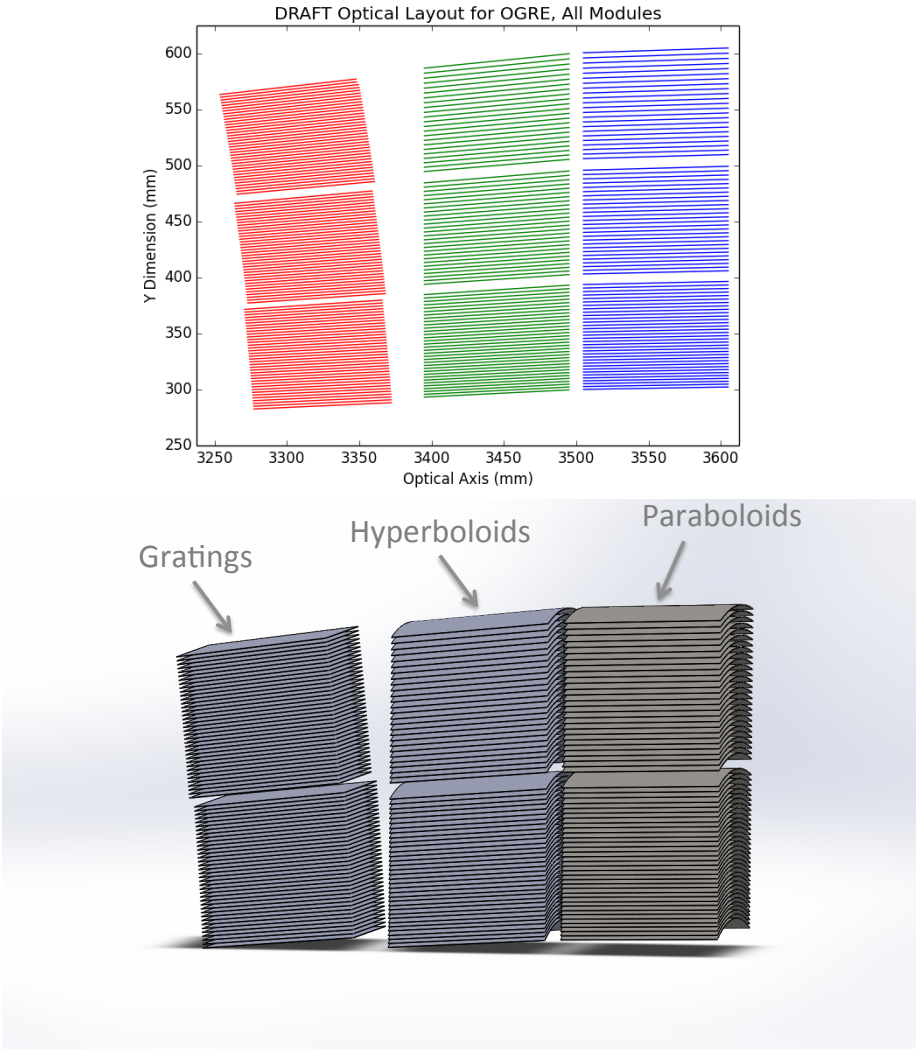

Figure 2.11: (*Top*) Rendering of a draft, three module optical design for the OGRE spectrometer. The paraboloid mirrors are shown in blue, hyperboloids in green, and gratings in red. In this representation, the optical elements are to scale. (*Bottom*) CAD rendering of this draft optical design.

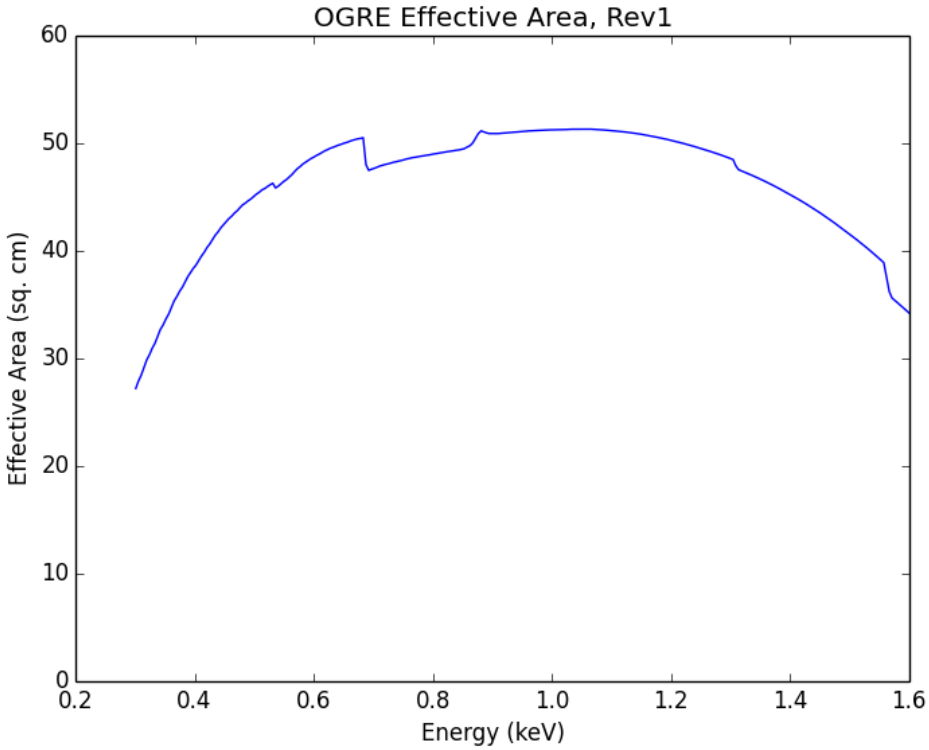

Figure 2.12: The effective area of the draft OGRE optical design as a function of photon energy.

Chapter 3

Work To Be Accomplished

For my thesis project, I anticipate accomplishing several more significant milestones along the road to the construction and flight of a cutting-edge grating spectrometer. For one, a theory of grating groove customization ought to be developed to guide the optimizaton process for future mission architectures. Next, the OGRE optical design ought to be completed in a timely fashion in order to guide the engineering effort already underway and provide process requirements for the OGRE flight gratings, mirrors, and detector. Finally, the OGRE gratings will need to fabricated, characterized, and aligned within a flight module within the next two years in order to stay on the current mission schedule.

3.1 Theory of Grating Customization

As the fabrication technique described in Subsection 2.1.2 enables the manufacture of gratings with a variety of groove densities and blaze angles, it remains to choose the optimal groove profile for the spectroscopy mission in question. It is well-known that the Littrow configuration yields the maximum diffraction efficiency for a given wavelength. From a broader mission standpoint, however, it is rare that a spectroscopy mission needs high efficiency at just a narrow range of wavelengths. Moreover, while the fabrication process itself is generalizable, in practice, constructing a variety of grating profiles for pre-mission evaluation is neither time- nor cost-effective. For instance, the grating imprint mold, from which the grating groove density is set, involves e-beam tooling which can require days of tool time and cost upwards of $100,000 to perform commercially. Hence, having the ability to quantitatively compare the diffraction efficiency of off-plane gratings prior to their fabrication (i.e. theoretically) is a necessity for future grating spectroscopy missions.

Calculations of the diffraction efficiency for gratings in a variety of mounting configurations, including the off-plane mount, have been performed by a number of different authors (see, for example, Loewen et al. (1977) , Goray and Seely (2002)). It is rare, however, that an author's published efficiency curve pertains to the grating comparison at hand. Our group purchased commerical software, *PCGrate*, which is capable of calculating grating diffraction efficiency for arbitary groove profiles. I used *PCGrate* to model the measured diffraction efficiency of the grating mold, but was unable to find a satisfactory fit to the mold efficiency data. The method *PCGrate* employs to calculate diffraction efficiencies is also somewhat ambiguous, owing in part to our lack of knowledge of diffraction theory. Achieving a more comprehensive understanding of the diffraction from first principles is a necessary first step to better utilize *PCGrate* and enable the comparison of diffraction efficiencies. This will be achieved by a literature review of grating efficiency calculations, and result in a detailed theory section in my final thesis document.

Next, in order to base grating construction decisions on the calculated values, verfiying the accuracy of the *PCGrate* efficiencies is paramount. This can be accomplished in two ways: either by developing a robust way to fit the measured empirical values with *PCGrate* through reasonable[1] variations in the grating groove profile or writing my own script to calculate grating diffraction efficiencies. Both of these paths are informed by the previous literature review.

Finally, this method should be used to predict the efficiency of the OGRE flight gratings prior to their manufacture. In the ideal case, SEM/AFM measurements of the groove density, surface roughness, groove profile, etc. would be translated into appropriate input parameters and a range of possible efficiencies found. Subsequent efficiency measurements (see Section 3.4) will allow for side-by-side comparison – if the measured efficiencies fall within the predicted range, it will serve as strong evidence that method of calculation can be used to support manufacturing decisions in future missions. The comparison of theoretical and measured efficiencies will be incorporated into a larger paper describing the manufacture and testing of the OGRE flight gratings.

[1] 'reasonable' being within the errors offered by physical measurements of the grating in question. Scanning Electron Microscope (SEM) and Atomic Force Microscopy (AFM) measurements can constrain the grating groove profile.

3.2 OGRE Optical Design Optimization

While a workable OGRE optical design has been found, the optical configuration has yet to be optimized for OGRE performance. The current OGRE design was found by adjusting the outer radii of the three mirror modules to maximize the total geometric area of the telescope while maintaining spectral resolving powers of $R > 2000$. The limiting factor in obtaining higher effective areas via this optimization process is the payload diameter. The telescope was extended from the default mirror inner radius R_0 (300 mm) radially outward until reaching the payload exterior skin on one side; however, the default grazing incidence angle ($\gamma = 1.5°$), requires the offset of the entire telescope assembly from the side directly opposite the outermost mirror by $\sim$180 mm. This leaves 'empty' geometric area that could be used, but only by adjusting the grating incidence angle, the inner telescope radius, and/or the angle between the optical axis and the instrument axis. Optimizing the design beyond this point is a non-trivial problem, as these parameters are highly coupled to number of optics needed, the effective area yield per optical segment, the ultimate resolution of the telescope, etc. In this complex parameter space, finding an optical design that yields the highest possible performance is a problem ideally suited for the iterative approach of *SpectDesign*.

First, a suitable optimization metric must be defined. To do this, papers reporting previous observations of Capella will be consulted to find high science-yield and/or yet unresolved diagnostic lines. By factoring together the resolutions achieved at these wavelengths, as well as the number of photons that would be collected over the OGRE's short observation window, it is possible to create a metric that ensures maximal OGRE science return. Assessing this metric for a variety of optical designs is slightly more difficult. Changing R_0 and γ changes the location of the spectrometer focus relative to the optical modules, shifting the ideal location for optical module placement from iteration to iteration. Thus, new *SpectDesign* scripts will have to be written to dynamically construct the best spectrometer within the 'hard' bounds of the payload envelope given the current parameter values within the scan. As the diffraction efficiency will also change at different grating incidence angles, this optimization will also involve either 1) calculating the diffraction efficiency in situ, 2) consulting a preconstructed library of diffraction efficiencies via look-up tables, or 3) demonstrating that the diffraction efficiency does not change appreciably over the scan range of interest. Finally, as a check on the optimization routine, a full raytracing simulation of the OGRE spectrometer should be completed. Such a simulation should begin with an ideal source spectrum of Capella derived from the X-ray modeling package *XSpec*, and propagate those source photons through the final optical

design to yield a sample physical output at the focal plane. Ideally, this simulation would take into account real uncertainties in the instrument (optical misalignments within tolerance, X-ray split events, etc.) and during flight (off-axis pointing, pointing drift, etc.). Having such a script in hand would be a powerful tool for future missions, as well as leave the OGRE team well-equipped to assess the impact of any changes or engineering constraints that arise during construction of the payload.

3.3 Fabrication of a Flight-like Grating

The final optical design will dictate the precise requirements for the OGRE flight gratings. Nonetheless, the preliminary design has already elucidated several process requirements which will necessate the further development of the off-plane grating microfabrication technique so far employed. For one, the preliminary optical design shows that a facet angle $\sim 30^\circ$ will be needed to obtain high effective areas in focal plane locations farthest from zero order (and hence yielding the highest resolutions that would be measured by OGRE). This in turn means that OGRE flight gratings will ultimately be most similar to the fabrication process for <311> gratings. The OGRE groove densities will remain in the 6000 gr/mm range, as the OGRE focal plane is of limited extent (≈ 150 mm) and the higher dispersions afforded by increased groove density will only serve to decrease OGRE's bandpass while yielding little in increased resolving power. Finally, to maximize instrumental effective area, the OGRE gratings must measure approximately 100 mm along the optical axis by 150 mm wide in order to intercept all of the focused light of the mirror modules. The larger format requires moving to 6" diameter wafers, which may introduce added complexity to the spin coating, imprinting, and wet etching steps.

In addition, there are several new elements to be considered during the fabrication process in order to yield gratings of high fidelity. For one, a new series of grating molds must be manufactured to yield the correct convergence for OGRE. McEntaffer et al. (2013) describes the mold manufacturing process in detail; we will concern ourselves here only with the writing of the mold pattern. Upon reaching a final optical design, *SpectDesign* will output grating pattern that must then be transferred into a CAD design. This CAD design will then be input into an electron beam (e-beam) lithography tool and written on an ultra-flat fused silica substrate coated with chromium and photoresist. It is our intent to perform the e-beam writing in house with the new Raith Voyager e-beam tool, which has been purchased by the University of Iowa and will be installed by Spring 2015. Performing the e-beam lithography step in-house will yield significant cost savings ($\sim$\$100,000) for the OGRE mission. In addition, this experience enables the prototyping of gratings for future, larger

missions cheaply and quickly.

The OGRE grating fabrication process must consistently yield the same groove profile – to accomplish this, the silicon nitride hardmask must be consistent from sample to sample. A CVD coating of silicon nitride will not only have a more consistent thickness across the (now larger) imprinted area than the silicon nitride deposited via reactive ion sputtering, but should also offer better chemical resistance to the buffered HF solution. Moving to this industrial standard also decreases the number of processing steps performed at Iowa, decreasing time spent per wafer and putting more of the fabrication procedure in the hands of industrial partners[2]. Changing the hardmask may require recharacterizing the current CHF_3/O_2 RIE step, an issue I anticipate solving on smaller, less expensive <311> wafers first before moving to flight-like gratings.

A high fidelity flight grating will also necessitate better alignment of the T-NIL mold to the <110> direction of the substrate. KOH etch 'ledges' along the groove add to the surface roughness of the grating surface and contribute to scattering. Furthermore, the flat plateaus between angled facets strengthen the zero order signal at the expense of the diffracted orders; the highest diffraction efficiencies will be achieved by gratings without significant plateaus[3]. Yet the need for small plateaus increases the alignment precision needed to not etch under the silicon nitride hardmask. The current alignment technique is good enough to not grossly undercut the mask in most cases but is far from consistent: multiple <100> and <311> samples have been undercut despite being processed in an identical fashion as samples that yielded normal grating profiles.

To achieve better mold/substrate alignment, I propose to perform an initial KOH etch of a small section of the substrate prior to the first imprint step to determine the true orientation of the substrate's crystalline planes. To perform this alignment step, a layer of positive photoresist would first be put down over top of the substrate. Next, a specially shaped photomask would be used to expose the resist in an area of the substrate that will ultimately be outside the grating area. The photomask pattern would be a series of lines, overlapping in their center and angularly fanned in a circle, like the spokes of a wagon wheel. After UV exposure, the resist would be processed and the 'wagon wheel' transferred through the silicon nitride layer via

[2]A manufacturing process that largely involves the use of industrial partners is often considered a strength in astronomical mission proposals. Hence, by making the move now, it is possible to realize the aforementioned benefits as well as strengthen the proposal case for future missions.

[3]Compare Figure 2.2, the middle right inset vs. the bottom center inset. The bottom inset has almost no plateau between angled facets, while for middle right inset, the plateaus are approximately 30% of the groove spacing and do not contribute efficiently to diffraction.

RIE, taking care to ensure that the eventual hardmask layer is not etched during this step. A KOH etch step is then performed and the spokes examined under an optical microscope. As the spokes are radially fanned, a wide range of possible crystallographic orientations are probed. The spoke with the cleanest, least undercut etch then indicates the <110> direction to within the tolerance of the spoke fan angle. As the flat orientation does not vary within a specified wafer batch, it would be possible to buy an entire silicon ingot of the desired crystallographic orientation, perform the 'wagon wheel' etch for a random set of wafers in the batch, measure the relative angle between the 'clean' KOH etch groove and the wafer flat, and use this measurement to align the T-NIL imprint for each wafer in that batch. This technique has been demonstrated to achieve angular tolerances of 0.05° (Chang, 2004).

Fabricating the first OGRE flight grating represents a large portion of the here-outlined thesis work. First, the off-plane grating microfabrication process will be further refined using relatively cheap <311> 3" wafers. These wafers will be coated with a CVD silicon nitride layer and used to characterize and, if necessary, tweak, the CHF_3/O_2 RIE etch used to transfer the grating pattern down to the substrate. These wafers will also be used to study the alignment procedure of the grating mold to the substrate crystalline planes using the described 'wagon wheel' method. After successful development of a reliable alignment method, the entire process will be used to produce a completed <311> grating on silicon. The resulting grating will be characterized in terms of groove profile, facet roughness, lithographic fidelity, etc. and if appropriate, measured for diffraction efficiency and resolving power. At this point, the OGRE optical design will be finalized and an order for the 6" OGRE substrates placed. Meanwhile, the grating pattern will be rendered in CAD, written via e-beam lithography and sent on to LightSmyth, an industrial partner, for subsequent processing. In the meantime, the OGRE substrates will arrive, which will enable early studies of T-NIL resist thickness on 6" substrates, the characterization of the crystalline plane orientation via the 'wagon wheel' process, etc. LightSmyth will next return a series of OGRE-specific molds, which will then be used to fabricate the OGRE flight gratings using the developed process. Upon fabricating gratings with acceptable profiles, these will be shipped to Nanonex for the completion of Steps #9 and #10. After completion of the UV-NIL imprint and reflective coating, Nanonex will send the fused silica gratings to Sydor Optics, the vendor for the fused silica substrates, who will dice out the grating pattern from the substrate to yield rectangular flight gratings. I anticipate producing approximately 20 silicon gratings for OGRE, which will be used to produce 100 – 300 fused silica gratings. I also anticipate performing this work in two phases, such that I will receive several prototype gratings which have been processed all the way through the production

chain prior to the delivery of the bulk of the flight gratings.

3.4 Performance Testing of a Flight-like Grating

When fabricated, the OGRE flight gratings will be the most sophisticated X-ray off-plane gratings ever manufactured. As such, characterizing the performance of the fabricated gratings is not only important for OGRE, but an essential component in any program enabling the next generation of X-ray grating spectrometers. To that end, I will test the flight gratings for both diffraction efficiency and resolving power.

A test campaign to measure the diffraction efficiency testing of the OGRE flight gratings will be conducted at the Physikalisch-Technische Bundesanstalt (PTB) soft X-ray beamline at the BESSY II synchrotron (Laubis et al., 2009). X-ray radiation from the electron storage ring is sampled by the beamline, and a grating monochromator is used to tune the beam to a specified energy between 0.1 – 1.9 keV. The optic is mounted on a stage in the test chamber which has six degrees of freedom, a critical feature for aligning off-plane gratings for a given test configuration. A photodiode capable of scanning in two dimensions is then used to sample the focal plane. By selecting the beam energy, positioning the photodiode at the location of a given order, and measuring the response of the photodiode, the diffraction efficiency of the grating in all non-evanescent orders can be mapped over energy space. For the OGRE flight gratings, I will measure the diffraction efficiency of the gratings at the nominal (0° yaw) and in the Littrow configuration at the incidence angle specified by the OGRE design and at $\gamma = 1.5°$ in order to be directly comparable to previous grating efficiency measurements performed at BESSY (McEntaffer et al., 2013; Tutt et al., 2015)

Following the BESSY campaign, I will test the resolving power of an OGRE flight grating at the NASA Marshall Space Flight Center's Stray Light Facility (SLF). The SLF consists of an electron impact X-ray source, a 100 m long beamline to collimate the source flux, and a 10 m long, 3 m diameter instrument chamber to house configurations of X-ray optics. The OGRE flight gratings will be tested in conjunction with a prototype OGRE mirror module manufactured by GSFC, which will create a focused X-ray beam with a convergence angle matching that of the flight gratings. This will be the first resolution measurement with blazed off-plane gratings fabricated via the method described in Section 2.1.2. A summary of the flight grating fabrication, diffraction efficiency measurements, and resolution measurements will then be reported in a publication.

3.5 Construction of a OGRE Flight Module

The culmination of this thesis effort is the construction of one aligned and flight-ready grating module for the OGRE spectrometer. Studies of off-plane grating alignment into a single module (Marlowe et al., 2015; Allured et al., 2015) are underway, but have thus far not achieved full alignment of the arcs of diffraction at the focal plane nor aligned more than two gratings. Thus, while the construction of a flight grating module benefits significantly from previous endeavors, it nonetheless represents a significant step towards realizing a next generation X-ray grating spectrometer.

Constructing the flight module first requires the production of at least 20 – 40 fused silica gratings. The flight housing will also need to be designed and built. The grating module will be fabricated from a specialized material, likely either Kovar to minimize the thermal expansion of the module over the course of flight or silicon carbide to match the coefficient of thermal expansion of the gratings. The flight housing will have wide slots cut at the nominal position of each grating, allowing for the position and orientation of the gratings to be fine-tuned after gross placement. Next, the gratings need to be qualified before integration into a flight module, as the gratings will be permanently bonded to the module. The qualification process may take the form of a visual inspection for gratings with poor imprint fidelity, an optical figure measurement, or even a simplified X-ray diffraction measurement. Either after or during qualification, the angle between the grating pattern and the diced substrate edge will also need to be measured with an optical microscope. The UV-NIL imprint boundary can be seen with the naked eye and is parallel to the central groove of the grating pattern. Knowing this angular offset is essential to aligning the grating about its normal without X-ray testing.

Next, each individual grating must be inserted into the module and correctly aligned in three spatial (x, the dispersion direction, y, the cross-dispersion direction, and z, the optical axis) and three rotation dimensions (pitch, the grating incidence angle, roll, grating rotation in the xy plane, and yaw, rotation about the grating normal; see Figure 3.1). This is performed with a specialized grating alignment assembly (Figure 3.2) mounted to an optical bench. A hexapod stage with six degrees of freedom is employed to position the grating within its mounting slot in the flight module. The flight module itself is mounted to a translation and tilt assembly, which serves to index each grating slot in the flight module. A coordinate-measuring machine (CMM) and a theodolite sample the grating face to provide position/orientation information. Each grating will be held by a set of six alignment flexures bonded to the outer edges of the grating. These flexures are then bonded to the grating module itself via holes in the module exterior. This alignment apparatus will be assembled

in a cleanroom environment so as to keep the optics free of particulate and molecular contamination.

When the alignment of the flight gratings has been completed, the grating module will be aligned to the corresponding mirror module, and mark the completion one full set of OGRE optics. Next, a systems-level test of the single OGRE optical module will be completed, either in an evacuated rocket skin on-site or at a facility with a beamline of appropriate length. A beamline test would be preferred, as this offers the opportunity to test the OGRE optical configuration in a regime where the source distance is much longer than the focal length of the system, thus approximating an 'source at infinity' (like an astronomical source). However, traveling to a beamline requires a significant investment of personnel time, and may not be possible at that point in the mission schedule and/or prior to the conclusion of this research. Testing the OGRE optics within the evacuated exterior skin of the rocket payload is an acceptable alternative, provided that source is placed a sufficient distance away from the optics modules. Testing within the rocket skin allow will allow the use of the OGRE detectors and be the first systems-level test of the entire OGRE instrument.

3.6 Thesis Summary

To summarize, this thesis will yield the following five scientific contributions to the next generation of X-ray reflection grating spectrometers:

1. A theoretical study of grating groove customization, with the goal of guiding the design choices for future off-plane X-ray grating instruments

2. A completed optical design for a grating spectrometer using a fast X-ray telescope

3. A well-characterized fabrication method for making high-fidelity off-plane X-ray gratings at custom facet angles

4. Data showing the resolution and efficiency performance of an off-plane X-ray grating fabricated using the aforementioned technique

5. An aligned and characterized grating module for the OGRE sounding rocket flight

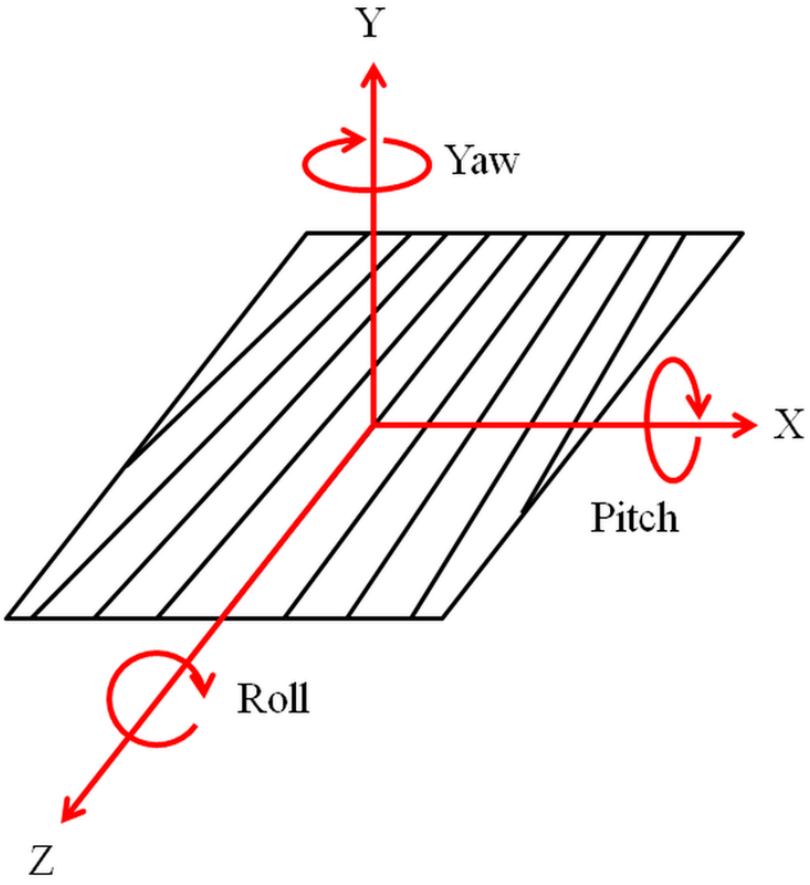

Figure 3.1: The grating coordinate system showing three spatial dimensions (x, y, z) and three rotational dimensions (pitch, roll, yaw).

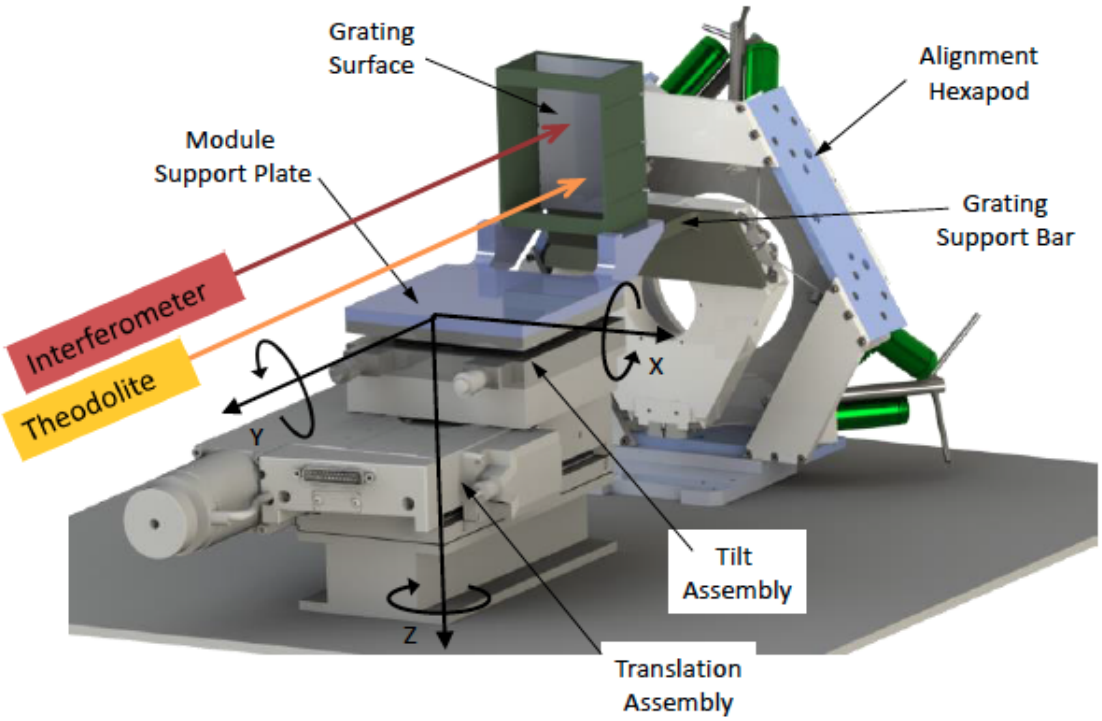

Figure 3.2: An example of a grating alignment assembly that could be used to position the OGRE gratings in the flight module. The CMM laser apparatus and theodolite are outside the picture, but can access the grating's optical surface.

Chapter 4

Proposed Timeline of Study

The thesis work described herein will be completed over the course of the next two years. An approximate schedule is as follows:

Spring 2015

- Complete analysis of first fabricated grating results (PANTER testing, see Section 2.2); write and publish paper.
- Optimize OGRE optical design and calculate nominal alignment tolerances; present finished design to OGRE instrument team
- Begin literature review of grating efficiency calculations

Summer 2015

- Characterize new CVD silicon nitride coating in grating fabrication process; develop new RIE recipe if required
- Develop new T-NIL mold alignment procedure
- Fabricate <311> grating using current ($z_0 = 8.4$ m) mold
- Translate OGRE grating pattern to CAD

Fall 2015

- Write OGRE grating pattern onto replication mask using Iowa e-beam lithography tool; send mask to LightSmyth for mold production
- Order silicon substrates for OGRE production
- Write grating efficiency calculation scripts; search for a reliable method of fitting measured efficiencies with theoretical models

- Simulate OGRE instrument response during 300 second observation of Capella, derive alignment tolerances through *SpectDesign* scripting

Winter 2015

- Receive OGRE substrates and grating molds
- Fabricate flight-like OGRE grating on silicon
- Design flight grating module and grating module alignment apparatus
- Conclude theoretical modeling work; publish if appropriate

Spring 2016

- Send silicon flight-like grating to Nanonex/Sydor Optics for completion; receive flight-like fused silica OGRE gratings
- Begin mass-production of flight-like OGRE gratings on silicon
- Measure diffraction efficiency of flight-like OGRE grating on fused silica
- Manufacture and assemble OGRE grating module, grating module alignment apparatus

Summer 2016

- Measure resolving power of flight-like, fused silica OGRE gratings
- Receive mass-produced, fused silica OGRE gratings from Nanonex/Sydor Optics
- Develop qualification method for fused silica OGRE gratings; measure angle between imprint and diced edge
- Study grating alignment technique using grating module alignment apparatus, engineering modules

Fall 2016

- Align fused silica OGRE gratings into grating module

Winter 2016

- Finish construction and alignment of OGRE grating module
- Begin writing dissertation

Spring 2017

- Measure the performance of the integrated OGRE optics module at suitable facility
- Finish writing dissertation
- Defend and graduate

Bibliography

Allured, R., Donovan, B., Burwitz, V., DeRoo, C., Marlowe, H., Menz, B., Miles, D., Tutt, J., and McEntaffer, R.: 2015, *forthcoming*

Allured, R. and McEntaffer, R. T.: 2013, *Experimental Astronomy* **36**, 661

Bavdaz, M., Wille, E., Wallace, K., Shortt, B., Collon, M., Ackermann, M., Riekerink, M. O., Haneveld, J., van Baren, C., Erhard, M., Christensen, F., Krumrey, M., and Burwitz, V.: 2012, in *Society of Photo-Optical Instrumentation Engineers (SPIE) Conference Series*, Vol. 8443 of *Society of Photo-Optical Instrumentation Engineers (SPIE) Conference Series*, p. 29

Born, M. and Wolf, E.: 1999, *Principles of Optics*, Cambridge University Press, 7$^{\text{th}}$ edition

Bregman, J. N.: 2007, *Annual Review of Astronomy and Astrophysics* **45**, 221

Cash, Jr., W. C.: 1983, *Applied Optics* **22**, 3971

Cash, Jr., W. C.: 1991, *Applied Optics* **30**, 1749

Chandra Project Science, MSFC: 2014, *The* Chandra *Proposers' Observatory Guide*, *Chandra* X-ray Center, 60 Garden Street, Cambridge MA 02138, Version 17.0

Chang, C.-H.: 2004, *Master's thesis*, Massachusetts Institute of Technology

den Herder, J. W., Brinkman, A. C., Kahn, S. M., Branduardi-Raymont, G., Thomsen, K., Aarts, H., Audard, M., Bixler, J. V., den Boggende, A. J., Cottam, J., Decker, T., Dubbeldam, L., Erd, C., Goulooze, H., Güdel, M., Guttridge, P., Hailey, C. J., Janabi, K. A., Kaastra, J. S., de Korte, P. A. J., van Leeuwen, B. J., Mauche, C., McCalden, A. J., Mewe, R., Naber, A., Paerels, F. B., Peterson, J. R., Rasmussen, A. P., Rees, K., Sakelliou, I.,

Sako, M., Spodek, J., Stern, M., Tamura, T., Tandy, J., de Vries, C. P., Welch, S., and Zehnder, A.: 2001, *Astronomy & Astrophysics* **365**, L7

DeRoo, C. T., McEntaffer, R. L., Schultz, T., Zhang, W. W., Murray, N. J., O'Dell, S. L., and Cash, W.: 2013, in *Society of Photo-Optical Instrumentation Engineers (SPIE) Conference Series*, Vol. 8861 of *Society of Photo-Optical Instrumentation Engineers (SPIE) Conference Series*

Goray, L. I. and Seely, J.: 2002, *Applied Optics* **41(7)**, 1434

Kendall, D. L.: 1975, *Applied Physics Letters* **26(4)**, 195

Laubis, C., Scholze, F., Bucholz, C., Fischer, A., Hesse, S., Kampe, A., Puls, J., Stadelhoff, C., and Ulm, G.: 2009, in *Society of Photo-Optical Instrumentation Engineers (SPIE) Conference Series*, Vol. 7271 of *Society of Photo-Optical Instrumentation Engineers (SPIE) Conference Series*

Loewen, E. G., Nevière, M., and Maystre, D.: 1977, *Applied Optics* **16(10)**, 2711

Marlowe, H., Allured, R., DeRoo, C., Miles, D., Donovan, B., Tutt, J., Menz, B., Burwitz, V., Hartner, G., and McEntaffer, R.: 2015, *forthcoming*

McEntaffer, R., DeRoo, C., Schultz, T., Gantner, B., Tutt, J., Holland, A., O'Dell, S., Gaskin, J., Kolodziejczak, J., Zhang, W. W., Chan, K.-W., Biskach, M., McClelland, R., Iazikov, D., Wang, X., and Koecher, L.: 2013, *Experimental Astronomy* **36**, 389

McEntaffer, R. L.: 2015, *forthcoming*

Smith, R. K.: 2014a, in *AAS/High Energy Astrophysics Division*, Vol. 14 of *AAS/High Energy Astrophysics Division*

Smith, R. K.: 2014b, *Arcus: Exploring the Formation and Evolution of Clusters, Galaxies, and Stars*, NASA Small Explorer Proposal

Tutt, J. H., Marlowe, H., Miles, D., Allured, R., and McEntaffer, R. L.: 2015, *forthcoming*

Tutt, J. H., McEntaffer, R. L., DeRoo, C., Schultz, T., Miles, D. M., Zhang, W., Murray, N. J., Holland, A. D., Cash, W., Rogers, T., O'Dell, S., Gaskin, J., Kolodziejczak, J., Evagora, A. M., Holland, K., and Colebrook, D.: 2014, in

Society of Photo-Optical Instrumentation Engineers (SPIE) Conference Series, Vol. 9154 of *Society of Photo-Optical Instrumentation Engineers (SPIE) Conference Series*

Zhang, W. W., Biskach, M. P., Bly, V. T., Carter, J. M., Chan, K. W., Gaskin, J. A., Hong, M., Hohl, B. R., Jones, W. D., Kolodziejczak, J. J., Kolos, L. D., Mazzarella, J. R., McClelland, R. S., McKeon, K. P., Miller, T. M., O'Dell, S. L., Riveros, R. E., Saha, T. T., Schofield, M. J., Sharpe, M. V., and Smith, H. C.: 2014, in *Society of Photo-Optical Instrumentation Engineers (SPIE) Conference Series*, Vol. 9144 of *Society of Photo-Optical Instrumentation Engineers (SPIE) Conference Series*

Appendices

Appendix A

Microfabrication Recipe for Off-Plane Gratings

The fabrication recipe presented here has gone through many iterations; presented here is the recipe used to make the <311> and <111> 10° off-axis wafers which were tested at PANTER. As outlined in Section 3.3, this recipe will need to be updated prior to the manufacture of the OGRE flight gratings. Specific UIMF tools are referenced, where appropriate.

1. Using Nanochrome I Sputterer, deposit silicon nitride layer.
   - Ion Source Ar: 5.5
   - Ion Source O_2: 0
   - Ion Source N_2: 8
   - Discharge I: 1.0 A
   - Discharge V: 120 V
   - Emission I: 1.25 A
   - Deposition Time: 5.0 min
   - Resulting thickness = 50 nm
2. Using spin coater, deposit NXR-1025 5.0% T-NIL resist.
   - 2-3 mL of resist sufficient for a 3" wafer
   - Spin speed: 4000 RPM
   - Ramp: 3000 RPM/sec
   - Resulting thickness = 95 nm

3. Soft bake-out of T-NIL resist.
    - Temperature: 120° C
    - Duration: 5 min
4. Using Nanonex NX-1000, imprint grating mold pattern with T-NIL step.
    - Clean treated mold with acetone, methanol, and isopropanol rinse, N_2 to dry
    - Orient grating mold along <110> direction
    - Preliminary pressure: 130 psi
    - Imprint temperature: 130° C
    - Imprint pressure: 200 psi
5. Using Oxford NGP-80, RIE T-NIL resist.
    - O_2: 10.0 sccm
    - Ar: 5.0 sccm
    - Power: 40 W RF
    - Operating pressure: 10 mTorr
    - Strike: 70 mTorr
    - Process Time: 75 sec
6. Using Oxford NGP-80, RIE silicon nitride layer.
    - O_2: 10.0 sccm
    - CHF_3: 50.0 sccm
    - Power: 150 W RF
    - Operating pressure: 100 mTorr
    - Process Time: 38 sec
7. Strip remaining T-NIL via acetone soak.
    - Agitation spin: 200 RPM
    - Process duration: 5.0 minutes
8. Remove native silicon dioxide via buffered HF dip.
    - Solution concentration: 16% ammonium fluoride in H_2O
    - Acid concentration: 49% HF
    - Mix in 20:1 ratio (solution : acid)
    - Process duration: 5 sec
9. Etch silicon substrate with KOH.

- KOH solution: 20% by weight
- Temperature: 20° C
- Process duration: 20 sec

10. Halt etch via H_2O soak.
    - Agitation spin: 200 RPM
    - Process duration: 3.0 min
11. Remove silicon nitride layer via concentrated HF soak.
    - Acid concentration: 49% HF
    - Process duration: 3.0 min
12. Rinse residual HF from substrate.
    - Solution: H_2O
    - Agitation spin: 200 RPM
    - Process duration: 3.0 min
13. Clean substrate of particulate.
    - Acetone spray rinse
    - Pressurized (80 psi) N_2 flow over substrate